




## Open Archive TOULOUSE Archive Ouverte (OATAO)

OATAO is an open access repository that collects the work of Toulouse researchers and makes it freely available over the web where possible.

This is an author-deposited version published in: <http://oatao.univ-toulouse.fr/>  
Eprints ID : 19541

**To link to this article** : DOI:10.1016/j.neuroimage.2010.10.040  
URL : <https://doi.org/10.1016/j.neuroimage.2010.10.040>

**To cite this version :**

Lorthoix, Sylvie  and Cassot, Francis and Lauwers, Frédéric  
*Simulation study of brain blood flow regulation by intra-cortical arterioles in an anatomically accurate large human vascular network. Part II: Flow variations induced by global or localized modifications of arteriolar diameters.* (2011) *NeuroImage*, vol. 54 (n° 4). pp. 2840-2853. ISSN 1053-8119

Any correspondence concerning this service should be sent to the repository administrator: [staff-oatao@listes-diff.inp-toulouse.fr](mailto:staff-oatao@listes-diff.inp-toulouse.fr)

# Simulation study of brain blood flow regulation by intra-cortical arterioles in an anatomically accurate large human vascular network. Part II: Flow variations induced by global or localized modifications of arteriolar diameters

S. Lorthois <sup>a,\*</sup>, F. Cassot <sup>b</sup>, F. Lauwers <sup>b,c</sup>

<sup>a</sup> Institut de Mécanique des Fluides de Toulouse, UMR CNRS/INP/UPS 5502, Allée du prof. C. Soula 31400 Toulouse, France

<sup>b</sup> Functional Neuroimaging Laboratory, INSERM U825, CHU Purpan, 31059 Toulouse Cedex 3, France

<sup>c</sup> Department of Anatomy, LSR 44, Faculté de Médecine Toulouse-Purpan, 133 route de Narbonne, 31062 Toulouse Cedex, France

## ARTICLE INFO

## ABSTRACT

In a companion paper (Lorthois et al., *Neuroimage*, in press), we perform the first simulations of blood flow in an anatomically accurate large human intra-cortical vascular network (~10000 segments), using a 1D non-linear model taking into account the complex rheological properties of blood flow in microcirculation. This model predicts blood pressure, blood flow and hematocrit distributions, volumes of functional vascular territories, regional flow at voxel and network scales, etc. Using the same approach, we study flow reorganizations induced by global arteriolar vasodilations (an isometabolic global increase in cerebral blood flow). For small to moderate global vasodilations, the relationship between changes in volume and changes in flow is in close agreement with Grubb's law, providing a quantitative tool for studying the variations of its exponent with underlying vascular architecture. A significant correlation between blood flow and vascular structure at the voxel scale, practically unchanged with respect to baseline, is demonstrated. Furthermore, the effects of localized arteriolar vasodilations, representative of a local increase in metabolic demand, are analyzed. In particular, localized vasodilations induce flow changes, including vascular steal, in the neighboring arteriolar trunks at small distances (<300  $\mu\text{m}$ ), while their influence in the neighboring veins is much larger (about 1 mm), which provides an estimate of the vascular point spread function. More generally, for the first time, the hemodynamic component of various functional neuroimaging techniques has been isolated from metabolic and neuronal components, and a direct relationship with several known characteristics of the BOLD signal has been demonstrated.

### Keywords:

Cerebral microcirculation  
Cerebral blood flow  
Neuroimaging  
BOLD signal  
Vascular point spread function  
Hemodynamic component  
Negative BOLD  
Calibrated fMRI

## Introduction

There is increasing recognition that, by its structural implication in neuro-vascular coupling, underlying vascular architecture is a key player in hemodynamically based functional imaging techniques (including fMRI and PET) (Harrison et al., 2002; d'Esposito et al., 2003; Logothetis and Wandell, 2004; Lauwers et al., 2008; Weber et al., 2008). In particular, the spatial resolution and specificity of such techniques are bound to the density of blood capillary vasculature and blood flow regulating structures (Harel et al., 2006). This is especially important in the context of high field fMRI (Duong et al., 2001; Harel et al., 2006), because, despite a dramatic increase in the theoretical spatial resolution obtained by using higher magnetic fields, associated with other hardware advancements, "the spatial extent of the hemodynamic response ultimately will impose a fundamental limitation on the spatial resolution of fMRI modalities" (Duong et al., 2001).

However, little is known about the fundamentals of the relationship between vascular structure and hemodynamic changes induced by brain activation. A growing body of evidence indicates that neurons, glia, and cerebral blood vessels, acting as an integrated unit, have a crucial role in mediating these activation-induced changes (Iadecola, 2004). In particular, the smooth muscle cells surrounding the arterioles, and possibly pericytes (Peppiatt et al., 2006; Fernández-Klett, 2008), at capillary level, convert the bio-chemical signals that originate from this integrated unit into changes in vascular diameter, thus regulating blood flow by modulating their vascular resistance. As argued in a companion paper (Lorthois et al., *Neuroimage*, in press), fluid dynamic modeling can be used to gain insight into brain blood flow regulation by intra-cortical arterioles, based on quantitative morphometric and topological data previously acquired on a large volume of the healthy human vasculature (Cassot et al., 2006).

The aim of the present paper is therefore to study spatial flow reorganizations induced by arteriolar vasodilations, in various configurations relevant to functional neuroimaging. First, flow reorganizations induced by global arteriolar vasodilations, i.e., simultaneous vasodilations of every arteriole in the network, will be analyzed. Studying such global vasodilations can provide information to help separate the vascular

\* Corresponding author. Fax: +33 5 34 32 29 93.  
E-mail address: lorthois@imft.fr (S. Lorthois).

component of the signal from other components directly related to brain activity (Thomason et al., 2005). This same idea is used in functional neuroimaging when hypercapnia is used to induce an isometabolic global increase in cerebral blood flow (Rostrup et al., 2000), in order to provide a calibration reference for fMRI studies (Davis et al., 1998; Ances et al., 2008). Second, following Boas et al. (2008), the effects of localized arteriolar vasodilations, representative of a local increase in metabolic demand (neuro-vascular coupling), will be analyzed with a particular attention to the effects of the underlying vascular architecture. In particular, the spatial extent (point spread function) of the induced hemodynamic changes will be studied. In fact, it is still uncertain whether these changes are sufficiently localized in the actual areas of elevated neuronal activity to resolve submillimeter functional units of the cortex, such as cortical orientation columns (Duong et al., 2001). In addition, emerging spatial patterns such as the vascular steal phenomenon (or surround negativity) (Devor et al., 2007; Boas et al., 2008; Harel et al., 2002; Woolsey et al., 1996; Cox et al., 1993; Kennerley et al., 2007) will be investigated.

## Methods

The methodology for simulating blood flow in the intra-cortical vascular network of a secondary cortex region extending over 7.7 mm<sup>2</sup> along the lateral part of the collateral sulcus (fusiform gyrus) has been presented in detail and validated in a companion paper (Lorthois et al., Neuroimage, 2011). Briefly, the network topology is represented by a connectivity diagram with edges of prescribed diameter and length. Given this topology diagram, a uni-dimensional (electrical analogy) non-linear network model has been slightly modified from Pries et al. (1990) to handle large networks. The model takes into account the complex rheological properties of blood flow in the microcirculation (i.e., Fahraeus, Fahraeus-Lindquist and phase separation effects). It is used to calculate the flow and hematocrit in each segment and the pressure at each node. Of course, the computed values of these parameters depend on the boundary condition prescribed at capillary nodes, and two relevant conditions, providing a lower- and upper-bound limit to the network behavior, have been determined: a zero-flow condition (Case 1) and a self-consistent constant pressure condition adjusted such that the net flux contributed by all the boundary capillary segments is null (Case 2).

The results can be analyzed from different points of view. First, the computed parameters can be analyzed without further treatment by studying their frequency distributions, spatial maps or dependence on each other. Second, these data can be *averaged* over parallelepiped regions of interest (ROIs) of depth equal to the depth of the thick section. Finally, integrated quantities, i.e., quantities characterizing blood flow *at the scale of the network*, can be calculated. For example, regional blood flow is calculated as the sum of the flows entering the domain through boundary nodes. Mean transit time is calculated as total blood volume divided by regional blood flow. Mean erythrocyte transit time is calculated as total erythrocyte volume divided by regional erythrocyte flow. Regional erythrocyte flow equals regional blood flow multiplied by inlet discharge hematocrit (a uniform value,  $H^{in}$ , is prescribed at the main arteriolar trunks as indicated in the companion paper). However, calculating the total erythrocyte volume is not so straightforward, because the tube hematocrit, rather than the discharge hematocrit, must be known. Thus, in each vessel, the tube hematocrit ( $h_{ij}$ ) is evaluated from the discharge hematocrit ( $H_{ij}$ ) using a parametric description of the Fahraeus effect developed from experiments on human red blood cell perfusion through glass tubes of different diameters ( $d_{ij}$ ) (Chien et al., 1984; Pries et al., 1990):

$$\frac{h_{ij}}{H_{ij}} = H_{ij} + (1 - H_{ij}) \cdot (1 + 1.7e^{-0.35d_{ij}} - 0.6e^{-0.01d_{ij}}). \quad (1)$$

Finally, the network Fahraeus effect corresponds to the ratio of the mean erythrocyte transit time to mean blood transit time.

## Active variations of the diameter of arteriolar trees

In order to study the active role of intra-cortical arterioles in the regulation of brain blood flow, diameter variations are assigned to either every arteriolar tree (global) or to one only (localized) by multiplying the diameter of all its segments down to a given diameter  $d_{vaso}$  by a constant factor  $f_{vaso}$ . Note that, in the case of localized arteriolar vasodilations, the adjusted constant pressure boundary condition (Case 2) becomes irrelevant, because it is no longer possible to assume that the net flux leaving the studied brain region through capillaries to supply neighboring areas is exactly compensated by the net flux arriving from neighboring areas through capillaries. In this case, increased outflow to the neighboring regions from the vascular territory of the vasodilated artery would be compensated by increased inflow from neighboring regions outside its vascular territory, which is clearly non-physiological. As a consequence, in the case of localized vasodilations, the zero-flow condition (Case 1) is the only condition studied. Calculations are repeated 11 times (i.e., for each arteriolar trunk) by “vasodilating” a different trunk each time.

## Passive variations of the diameter of venular trees

The modifications in venous pressure induced by global arterial vasodilations induce a passive *balloon* expansion of the venous volume (Buxton et al., 1998). In order to estimate this effect, a non-linear compliance producing a venous pressure volume relationship of the form:

$$P - P_{IC} = \left( \frac{V}{A_0} \right)^\beta, \quad (2)$$

can be introduced following Boas et al. (2008). In this expression  $P_{IC}$  is the intra-cranial pressure, assumed to be constant (10 mmHg),  $\beta = 2$  as a representative of the range  $1 < \beta < 3$  given in the literature and  $A_0$  is a constant.

With this expression, it is possible to deduce the venous vasodilation factor ( $f_v = \frac{r(f_{vaso})}{r(f_{vaso}=1)}$ , i.e., the ratio between the vasodilated venous radius and the baseline venous radius):

$$f_v = \left( \alpha + (\alpha - 1) \frac{P_{IC}}{P(f_{vaso}=1) - P_{IC}} \right)^{1/(2\beta)}, \quad (3)$$

$\alpha$  being the relative pressure variation  $\frac{P(f_{vaso})}{P(f_{vaso}=1)}$ . Because the venous mean baseline pressure decreases with increasing vessel radius (see Companion Paper, Fig. 2), this venous vasodilation factor is dependent on the baseline vessel radius. In a series of computations (as indicated in text), in addition to global arteriolar vasodilations, diameter variations have been prescribed to all venular segments by multiplying their baseline diameter by the corresponding value of  $f_v$ . Note that, with this approach, the effect of passive venular vasodilations is overestimated, because the process is not repeated until convergence of the venous diameter and pressure values. However, this approach is useful to estimate how passive venous vasodilation would affect hemodynamic variations at network scale.

## Analysis of hemodynamic variations

In the case of global vasodilations, the variations of regional blood flow  $Q_r$ , mean capillary pressure  $\bar{P}_c$ , blood volume  $V_r$  and mean transit time  $\bar{t}_r$  as a function of  $f_{vaso}$  are analyzed by considering the flow in two equivalent resistances in series due to a constant pressure drop  $\Delta P$  (60 mmHg) (Fig. 1). According to Poiseuille's law, the first resistance,  $R$ , is a function of  $f_{vaso}$ :

$$R(f_{vaso}) = R_0 \cdot f_{vaso}^{-4}. \quad (4)$$

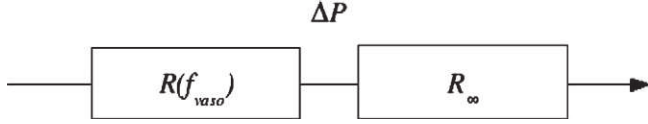


**Fig. 1.** Simplified description of the intra-cortical network under study by two equivalent resistances in series submitted to a constant pressure drop  $\Delta P$  (60 mmHg). The first resistance is variable and represents the arteriolar part of the network. It is proportional to the vasodilation factor to the power 4 (Poiseuille's law). The second resistance is constant and represents the capillary and venular parts of the network.

whereas the second resistance,  $R_\infty$ , is constant. In addition, the blood volume corresponding to each resistance is assumed to scale as  $V_0 \cdot f_{vaso}^2$  and  $V_\infty$ , respectively. In this framework:

$$Q_r = \Delta P / (R_0 \cdot f_{vaso}^{-4} + R_\infty), \quad (5)$$

$$V_r = V_0 \cdot f_{vaso}^2 + V_\infty, \quad (6)$$

$$\bar{t}_r = (V_0 \cdot f_{vaso}^2 + V_\infty) (R_0 \cdot f_{vaso}^{-4} + R_\infty) / \Delta P, \quad (7)$$

$$\bar{P}_c = P_v + R'_\infty \cdot Q_r, \quad (8)$$

where  $P_v$  is the outlet venous pressure and  $R'_\infty$  is the unknown resistance downstream of the capillaries ( $R'_\infty < R_\infty$ ). The values of the equivalent resistances  $R_0$ ,  $R_\infty$  and  $R'_\infty$ , of the blood volumes  $V_0$  and  $V_\infty$ , as well as the

values of the outlet venous pressure  $P_v$  are obtained by adjusting the results to the above equations using non-linear least-square interpolation. Finally, in order to extract figures for physical interpretation, the diameters  $d_0$ ,  $d_\infty$  and  $d'_\infty$  of 50  $\mu\text{m}$  long segments with the same equivalent resistance as  $R_0$ ,  $R_\infty$  and  $R'_\infty$ , respectively, are calculated.

### Spatial dynamics of the flow changes

In order to evaluate the spatial dynamics of the flow changes induced by the localized vasodilation of a given arteriolar trunk ( $i$ ), both the magnitude and the spatial extent of the changes must be evaluated. For that purpose, the flow rate variations in every main arteriolar or venular trunk ( $j$ ) relative to baseline ( $\delta Q_{A,j}^i$  or  $\delta Q_{V,j}^i$ , respectively) are calculated for the maximal value of  $f_{vaso}$  under study ( $f_{vaso} = 2$ ). The results are plotted as a function of  $d_{ij}$ , the distance between  $i$  and  $j$  projected over the sulcus. In the same way, the variations in the volume of the territories fed or drained by each main arteriolar or venular trunk ( $j$ ), determined as described in part I, relative to baseline ( $\delta V_{A,j}^i$  or  $\delta V_{V,j}^i$ , respectively) are also plotted.

## Results

### Hemodynamic variations induced by global arteriolar vasodilations

#### Variations at network scale

The variations of network integrated parameters (regional blood flow, mean capillary pressure, blood volume, mean transit time, network

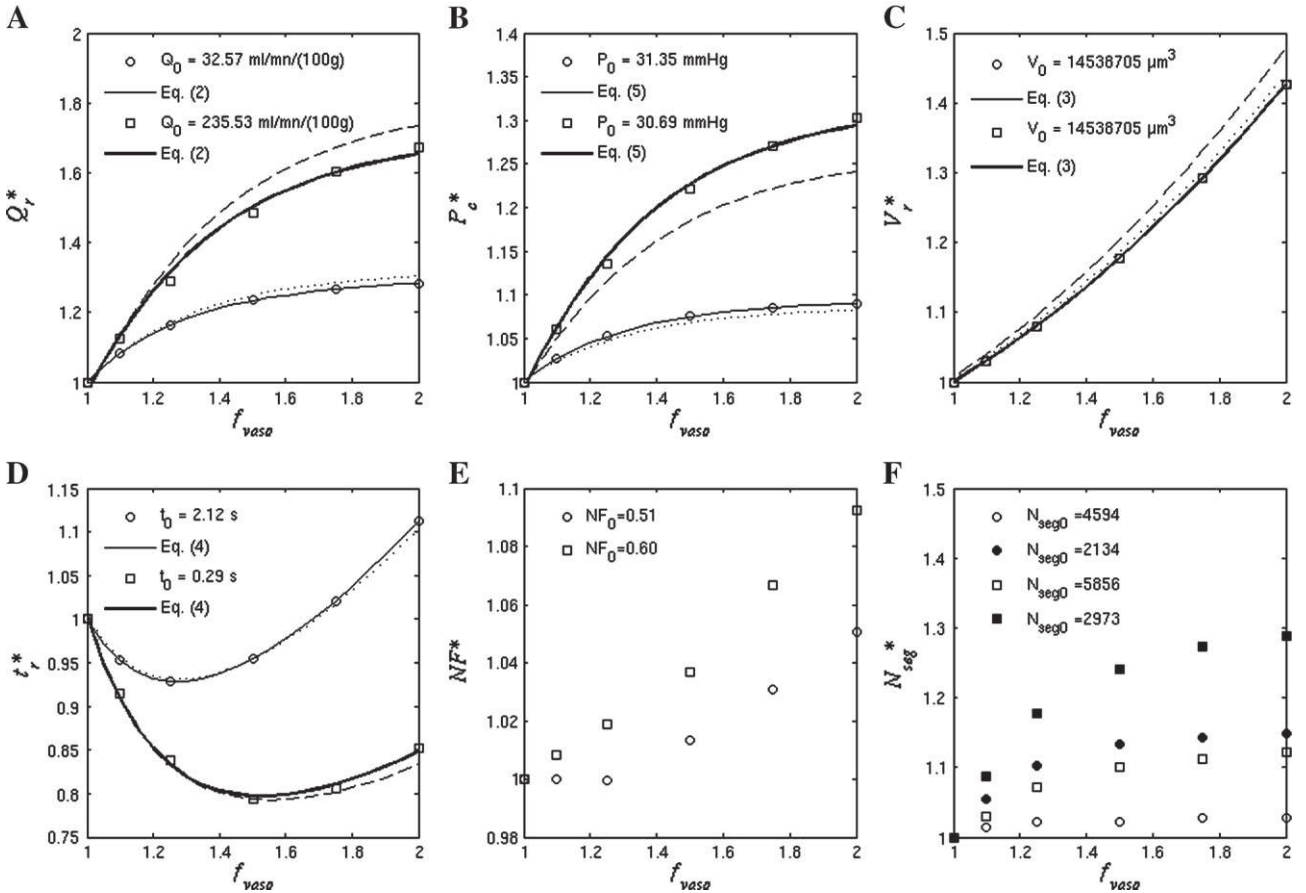


**Fig. 2.** Global vasodilations: network integrated parameters, normalized by their baseline value ( $f_{vaso} = 0$ ) as a function of vasodilation factor  $f_{vaso}$  ( $d_{vaso} = 9.9 \mu\text{m}$  and  $H^{in} = 0.4$ ). A: regional blood flow; B: mean capillary pressure; C: total blood volume; D: mean transit time; E: network Fahraeus effect (mean red blood cells transit time to mean blood transit time ratio); F: number of segments with flow above a given threshold (0.2 nl/min and 1 nl/min for open and filled symbols, respectively). Circles: Case 1 without passive venous vasodilation; Squares: Case 2 without passive venous vasodilation. Plain lines: best adjustment of the data computed without passive venous vasodilation according to Eqs. (5) to (8). Discontinuous lines: best adjustment of the results obtained by considering a passive venous vasodilation. Baseline values are indicated in the legend of each panel. The parameters deduced from least-square adjustment are displayed in Table 1 (no venous vasodilation) and Table 4 (effect of venous vasodilation).

**Table 1**

Parameters obtained by adjustment of the variation of network integrated parameters as a function of vasodilation factor  $f_{\text{vaso}}$  (see Fig. 2) using Eqs. (5) to (8).  $H^{\text{in}} = 0.4$ .

		Case 1		Case 2	
		$d_{\text{vaso}} = 9.9 \mu\text{m}$	$d_{\text{vaso}} = 14.9 \mu\text{m}$	$d_{\text{vaso}} = 9.9 \mu\text{m}$	$d_{\text{vaso}} = 14.9 \mu\text{m}$
$Q_r$ (Eq. (5))	$d_0$ ( $\mu\text{m}$ )	9.73	11.59	13.56	16.25
	$d_\infty$ ( $\mu\text{m}$ )	7.24	6.99	12.74	11.79
$\bar{P}_c$ (Eq. (8))	$P_v$ (mmHg)	21.49	21.03	17.27	16.19
	$d_\infty$ ( $\mu\text{m}$ )	10.63	10.52	16.11	15.84
$V_r$ (Eq. (6))	$V_0$ ( $\mu\text{m}^3$ )	2,063,051	1,067,719	2,063,051	1,067,719
	$V_\infty$ ( $\mu\text{m}^3$ )	12,475,653	13,470,985	12,475,653	13,470,985
$\bar{t}_r$ (Eq. (7))	$V_0$ ( $\mu\text{m}^3$ )	2,063,051	1,067,719	2,063,051	1,067,719
	$V_\infty$ ( $\mu\text{m}^3$ )	12,188,727	12,868,337	18,768,667	14,870,584
	$d_0$ ( $\mu\text{m}$ )	9.63	11.30	15.54	16.91
	$d_\infty$ ( $\mu\text{m}$ )	7.22	6.92	13.62	12.03

Fahraeus effect and number of vessels exhibiting flow above a given threshold) as a function of  $f_{\text{vaso}}$  and without passive venous vasodilation are displayed by symbols in Fig. 2. Whatever the integrated parameter under study, it is noteworthy that its qualitative behavior is independent of the boundary condition chosen (Case 1 or Case 2). Moreover, the initial rate of variation is always greater for Case 2 than for Case 1, which confirms that these two boundary conditions provide an upper and lower bound, respectively, for the hemodynamic behavior of the network under study. With regard to the quantitative description of this behavior, despite the oversimplified description of the network flow by two resistances in series, the adjustment of the calculated data to Eqs. (5) to (8) is very accurate, with correlation coefficients  $r$  always above 0.997 (continuous lines in Fig. 2). In addition, the parameters obtained by least-square interpolation of the numerical data using these different equations are consistent (see Table 1): the values of  $d_0$  and  $d_\infty$  obtained by fitting  $Q_r$  to Eq. (5) and  $\bar{t}_r$  to Eq. (7), respectively, are in close correspondence, especially when the zero-flow boundary condition is used. In the same way, the values of  $V_0$  and  $V_\infty$  obtained by fitting  $V_r$  to Eq. (6) and  $\bar{t}_r$  to Eq. (7), respectively, are also in reasonable agreement. Finally, the orders of magnitudes of these parameters, as well as their relative values, are meaningful, bearing physical significance:  $6.99 \mu\text{m} < d_\infty < d_0 < 16.25 \mu\text{m}$ . As a consequence, such an approach could be used to quantitatively study the global hemodynamic changes in various brain areas, seeking correlations between the extracted coefficients and their macroscopic architectural properties, for example their vascular densities.

From these results, the relationship between changes in volume and changes in flow, previously summarized as a power law ( $CBV = CBF^\phi$ ), can be investigated. Following Sheth et al. (2004a),  $\phi$  is the slope of the linear relationship:

$$\log(\delta CBV + 1) = \phi \cdot \log(\delta CBF + 1), \quad (9)$$

where  $\delta$  denotes baseline-normalized fractional change in the respective parameter. From Eqs. (5) and (6), however, it is clear that this linear relationship does not hold for all magnitudes of the flow and volume changes (Fig. SM1, Supplementary Material). However, it is possible to linearize these equations (series expansion) for small flow rate variations (i.e., when the range of  $f_{\text{vaso}}$  is restricted so that  $f_{\text{vaso}} = 1 + \varepsilon$ ,  $\varepsilon$  being a small parameter) in order to calculate  $\phi$ :

$$\phi = \frac{1}{2} \frac{V_0}{V_0 + V_\infty} \frac{R_0 + R_\infty}{R_0} \quad (10)$$

**Table 2**

Exponent on the power law ( $CBV = CBF^\phi$ ) obtained for small variations of the vasodilation factor ( $f_{\text{vaso}}$ ), i.e., small variations of blood flow and blood volume.  $H^{\text{in}} = 0.4$ .

	Case 1		Case 2	
	$d_{\text{vaso}} = 9.9 \mu\text{m}$	$d_{\text{vaso}} = 14.9 \mu\text{m}$	$d_{\text{vaso}} = 9.9 \mu\text{m}$	$d_{\text{vaso}} = 14.9 \mu\text{m}$
$\phi$	0.306	0.314	0.162	0.169

The corresponding numerical values (see Table 2) are in the range 0.16–0.30. This is in close accordance with the range 0.18–0.36 determined by several groups using recent techniques such as laser Doppler flowmetry and optical imaging in brain activation studies (Mandeville et al., 1999; Jones et al., 2001; Sheth et al., 2004a and references therein, Leung et al., 2009; Boas and Payne, 2009). Note that the original value  $\phi = 0.38$  was experimentally determined by Grubb et al. (1974) in PET studies using a prolonged hypercapnia challenge in primates.

In addition, it is interesting to note that the mean transit time variation is non-monotonic (Fig. 2D): an initial decrease in the mean transit time is observed because the blood volume initially increases more slowly than the regional blood flow (consistent with the values of  $\phi$  obtained above). For larger vasodilations, the regional blood flow levels off, which induces an increase of the mean transit time. By contrast, the network Fahraeus effect increases monotonically in a linear fashion (Case 2) or reaching a linear regime for larger vasodilations (Case 1), see Fig. 2E. In other words, the difference between mean erythrocyte transit time and mean blood transit time decreases monotonically, meaning that the mean erythrocyte velocity increases more slowly than the mean blood velocity. This effect tends to counterbalance the decrease in transit time at low vasodilations. All together, these variations in mean transit time and relative erythrocyte mean transit time are likely to induce variations in oxygen extraction potentially impacting the BOLD effect.

Finally, the number of low-flow capillaries decreases monotonically, with higher rates for small vasodilations of the arteriolar trees (Fig. 2F). This is evidenced by the increasing fraction of segments exhibiting flows over fixed thresholds. In order to allow a comparison with experimental data (Villringer et al., 1994), the mean red blood cell velocity and mean red blood cell flux in capillary vessels were calculated. Results are displayed in Table 3. Regarding the red blood cell velocity, experimental baseline values (normocapnia) are in between the values calculated by using boundary conditions Case 1 and Case 2, at baseline ( $f_{\text{vaso}} = 1$ ). In the same way, experimental hypercapnia values are in between the values calculated by using boundary conditions Case 1 and Case 2, at maximal vasodilation ( $f_{\text{vaso}} = 2$ ). However, the relative increase (14.3 and 36.8% using Case 1 and Case 2, respectively) is lower than the

**Table 3**

Mean red blood cell velocity and mean red blood cell flux in capillary vessels: quantitative comparison with Villringer's et al. (1994) results. Note that the arteriolar vasodilation factor ( $f_{\text{vaso}}$ ) is not precisely known during hypercapnia in this experimental study. Therefore, because the mean red blood cell velocity and flux flow reach an asymptotic regime, in the same way as the regional blood flow (see Discussion section), the comparison is made with the maximal value of  $f_{\text{vaso}}$  considered in the present work. ( $H^{\text{in}} = 0.4$ ,  $d_{\text{vaso}} = 9.9 \mu\text{m}$ ).

	Villringer et al.		Case 1		Case 2	
	Baseline	Hypercapnia	$f_{\text{vaso}} = 1$	$f_{\text{vaso}} = 2$	$f_{\text{vaso}} = 1$	$f_{\text{vaso}} = 2$
Velocity ( $\mu\text{m/s}$ )	519	828	427	488	628	859
Flux (cells/s)	39	55	65	83	103	196

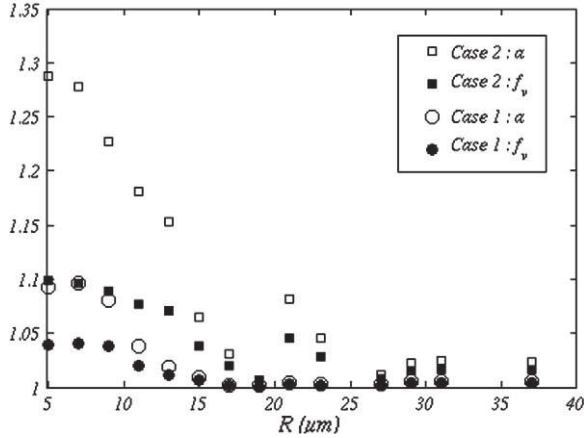


**Fig. 3.** Global vasodilations: pressure relative variation  $\alpha$  (closed symbols) and venous vasodilation factor  $f_v$  (open symbols) as a function of venular radius at maximal arterial vasodilation ( $f_{vaso} = 2$ ). In practice, pressure has been averaged over  $2 \mu\text{m}$  vessel radius ranges before computing these data.

experimental relative increase (59.5%). Regarding the absolute red blood cell flux, both boundary conditions over-estimate the experimental results, whereas the experimental flux relative variation (41.0%) is in between the variations calculated by using boundary conditions Case 1 and Case 2 (27.7% and 90.3%, respectively). These results are consistent with the concept of continuous perfusion of all brain capillaries (absence of capillary recruitment in an open/closed fashion), as introduced by Kuschinsky and Paulson (1992). However, the experimentally reported reduction in heterogeneity of capillary perfusion (Villringer et al., 1994; Vogel and Kuschinsky, 1996) is reproduced by our model only if boundary condition Case 2 is used. In this case, the coefficient of variation of capillary blood flow decreases from 4.6 (baseline) to 4.0 (maximal vasodilation), whereas it slightly increases in Case 1, from 1.6 to 1.7.

#### Variations at network scale: Modifications induced by passive venous vasodilations

In order to investigate the sensitivity of the variations at network scale described above to passive venous vasodilations, the relative pressure variations in veins,  $\alpha$ , and the venous vasodilation factor,  $f_v$ , must be calculated (Eq. (3)) for each value of  $f_{vaso}$ . Fig. 3 displays the results obtained for  $f_{vaso} = 2$ , demonstrating a strong decrease with increasing venous radius, and a maximal vasodilation of  $\sim 4\%$  (Case 1) or  $\sim 10\%$  (Case 2) in venules of  $5\text{--}6 \mu\text{m}$  radius.

The influence of these additional passive venous vasodilations superimposed to the active arterial vasodilations is illustrated in Fig. 2,

where the best fits of the results according to Eqs. (5) to (8) are displayed as discontinuous lines. As previously, the adjustment is very good, with correlation coefficients  $r$  always above 0.996. The qualitative behavior of the network is therefore unchanged when venous compliance is taken into account. As expected, the total blood volume and regional blood flow increase, whereas the capillary pressure decreases, compared to the results obtained with non-deformable veins. As a result, the mean transit time is practically unchanged. At the quantitative level, the augmentation of total volume induced by passive venous vasodilation is comprised between 1.05% (Case 1) and 3.71% (Case 2), whereas the flow rate augmentation is slightly larger [1.56% (Case 1) to 4.96% (Case 2)]. This demonstrates a small contribution of the passive venous response when remembering that our methodology provides over-estimates for this response. Moreover, exponent  $\phi$  in the power law between CBF and CBV remains in the same range [0.16–0.30] as previously, with values of 0.290 and 0.165 in Case 1 and Case 2, respectively (see Table 4).

#### Blood flow: Correlation with vascular structure?

In order to find out if the relationships between blood flow and vascular structure extracted for baseline conditions are modified by global vasodilations, the analyses performed in the companion paper are repeated for the maximal value of  $f_{vaso}$  under study ( $f_{vaso} = 2$ ). First, a power relationship between the flow rate in each vascular trunk (arteries and veins) and the volume of their territories, determined as described in part I, is sought (see Fig. SM2, Supplementary Material). In Case 1, Pearson's  $r$  coefficient is 0.62, indicating a weak correlation, with a high significance level of 0.005. In Case 2, a stronger correlation is observed ( $r = 0.77$  at a significance level of 0.001). These values are similar to the values obtained at baseline. Moreover, the exponent in the power relationship that maximizes the correlation ( $a = 0.43$ ) is independent of the boundary condition used and it is almost unchanged compared to the baseline coefficient ( $a = 0.46$ ).

In addition, a correlation between the flow in parallelepiped ROIs and the proportion of vascular space occupied by non-capillary vessels was also sought (see Fig. SM3, Supplementary Material). In  $250 \mu\text{m}$  ROIs, this correlation is weak but significant ( $p < 0.001$ ) for both boundary conditions used, with Pearson's  $r$  coefficients of 0.68 and 0.66 in Case 1 and case 2, respectively ( $n = 56$ ). In  $500 \mu\text{m}$  ROIs, this correlation is weak but significant ( $p < 0.025$ ) for both boundary conditions used, with Pearson's  $r$  coefficients of 0.67 and 0.71 in Case 1 and Case 2, respectively ( $n = 9$ ). As previously, results obtained in both kinds of ROIs are correctly matched after rescaling, demonstrating the relevance of the observed correlation which is indeed independent of the size of the ROI.

**Table 4**  
Influence of passive venous vasodilation on the parameters obtained by adjustment of hemodynamic behavior of the network in response to global arteriolar vasodilations (see Fig. 2) using Eqs. (5) to (8).  $H^{in} = 0.4$ .

$d_{vaso} = 9.9 \mu\text{m}$		Case 1			Case 2		
		No venous vasodilation	Passive venous vasodilation	Relative variation (%)	No venous vasodilation	Passive venous vasodilation	Relative variation (%)
$Q_r$ (Eq. (2))	$d_0$ ( $\mu\text{m}$ )	9.73	9.58	-1.56	13.56	13.28	-2.04
	$d_\infty$ ( $\mu\text{m}$ )	7.24	7.28	0.55	12.74	12.95	1.68
$P_c$ (Eq. (5))	$P_v$ (mmHg)	21.49	23.10	7.49	17.27	21.05	21.87
	$d_\infty$ ( $\mu\text{m}$ )	10.63	11.13	4.68	16.11	17.46	8.37
$V_r$ (Eq. (3))	$V_0$ ( $\mu\text{m}^3$ )	2,063,051	2,116,722	2.60	2,063,051	2,289,082	10.96
	$V_\infty$ ( $\mu\text{m}^3$ )	12,475,663	12,480,658	0.04	12,475,663	12,350,042	-1.01
$t_r$ (Eq. (4))	$V_0$ ( $\mu\text{m}^3$ )	2,063,051	2,116,722	2.60	2,063,051	2,289,082	10.96
	$V_\infty$ ( $\mu\text{m}^3$ )	12,188,727	13,543,884	11.12	20,946,870	26,893,283	28.39
$\phi$ (Eq. (10))	$d_0$ ( $\mu\text{m}$ )	9.63	9.95	3.32	15.54	17.14	10.30
	$d_\infty$ ( $\mu\text{m}$ )	7.22	7.37	2.05	13.62	14.71	8.00
	$\phi$	0.305	0.290	-4.93	0.162	0.165	1.87

### Spatial heterogeneities of the hemodynamic variations

The spatial heterogeneities of the hemodynamic variations are illustrated in Fig. 4. In this figure, each segment in the network is colored depending on the variation of its mean pressure, blood flow or hematocrit for the maximal value of  $f_{\text{vaso}}$  under study ( $f_{\text{vaso}} = 2$ ) relative

to baseline. The main result is the large spatial heterogeneity of the observed variations. For example, regarding pressure variations, even if the largest fraction of the network exhibits pressure increases, several spots exhibit pressure reductions (see arrows in Fig. 4), the number and extent of these spots being larger with Case 1 boundary condition

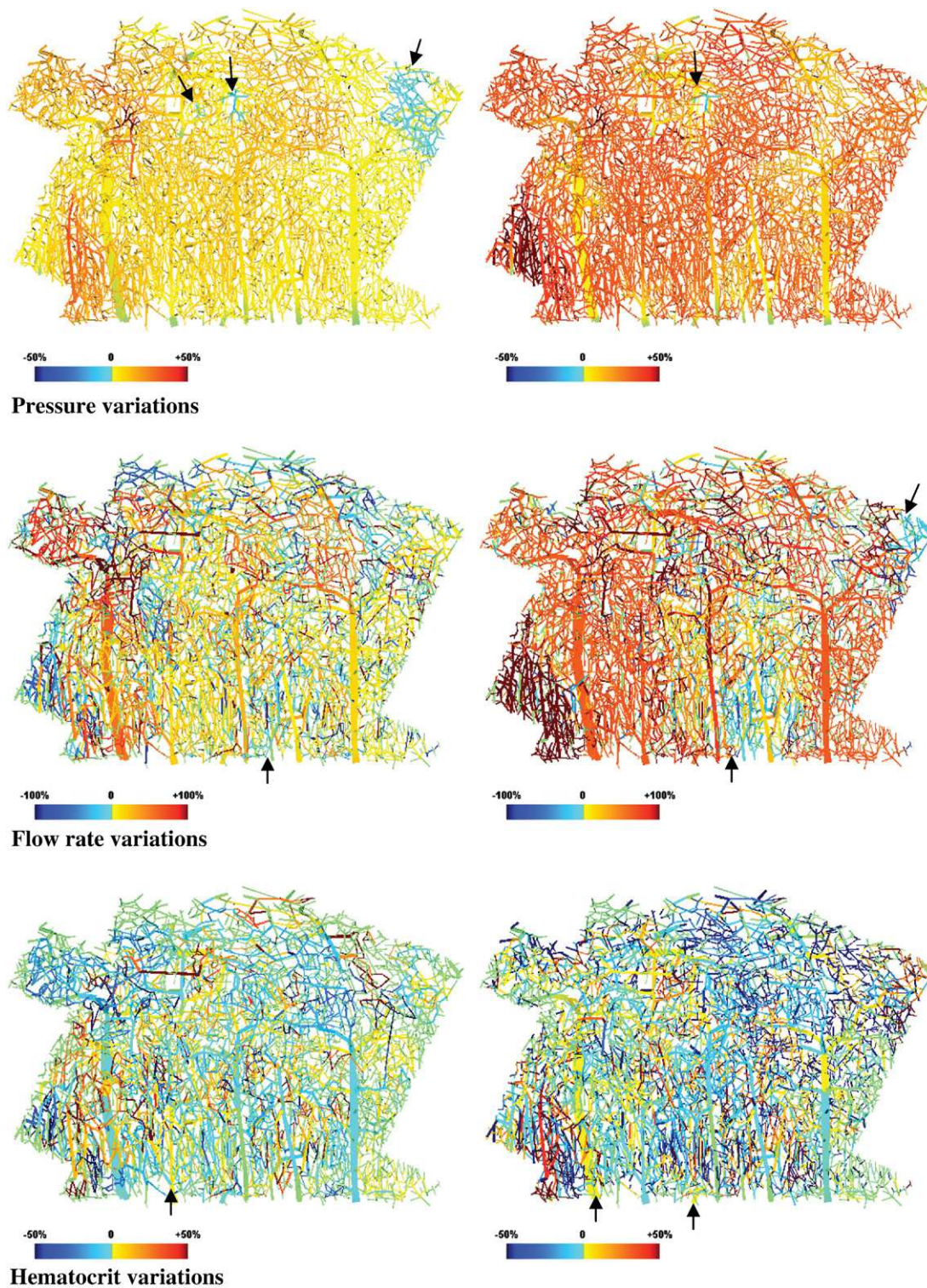


**Fig. 4.** Global vasodilations: spatial distributions of pressure variations (first row), flow rate variations (second row) and hematocrit variations (third row) calculated for the maximal value of  $f_{\text{vaso}}$  under study ( $f_{\text{vaso}} = 2$ ) relative to baseline for zero-flow (Case 1) boundary condition (left) and assigned pressure (Case 2) boundary condition (right) and  $H^{\text{H}} = 0.4$ . Numerical values of mean pressure variation and flow rate variation in each segment relative to baseline are color-coded as indicated in the color scale. For clarity of representation, diameters have been increased threefold compared to lengths. Hot colors (yellow to reddish) display positive variations whereas cold colors (bluish colors) display negative variations. Green segments are segments exhibiting no variation relative to baseline. For more details on arrows, see text. The normalized distributions corresponding to these maps are displayed in Fig. SM12.

(consistent with the reduced elevation of the mean network pressure, see Fig. 2). Regarding the flow rate variations, the majority of the main arteriolar trunks shows an increase in flow rate. However, several main arteriolar trunks of reduced size exhibit either no variation or even present a reduced flow rate (see arrows in Fig. 4). This result demonstrates that even with all cortical regions responding to the prescribed global vasodilation, some vascular steal processes are operative. The dispersion in flow rate variations is much smaller in the main venular trunks, which all exhibit a flow increase of the same order of magnitude. Finally, regarding hematocrit variations, the majority of large draining veins display a decrease in discharge hematocrit, with a few trunks (see arrows in Fig. 4) exhibiting an increase in hematocrit.

*Maximal vasodilation: Correlation of hemodynamic parameters with baseline parameters?*

First, the relationships between the hemodynamic parameters (blood flow and volume of the vascular territories) characterizing

each main arteriolar or venular trunk before and after a global vasodilation ( $f_{vaso}=2$ ) were sought. The results are displayed in Figs. SM4 and SM5 (Supplementary Material). Regarding the flow rate (Fig. SM4), the flow after maximal vasodilation is highly correlated with the baseline flow, in both arteriolar trunks and venular trunks. In Case 1, Pearson's  $r$  coefficients obtained when studying arterial and venous trunks separately are above 0.98 with high significance levels of less than 0.001. Moreover, the correlation is not weakened when arterioles and venules are studied as a single group. In Case 2, the correlations are slightly weaker when arterioles are considered separately ( $r=0.81$  at a significance level of 0.005) or when arterioles and venules are grouped ( $r=0.89$  at a significance level of 0.001). With regard to the volume of the vascular territories (Fig. SM5), strong correlations ( $r>0.93$ ) with high significance levels ( $p<0.001$ ) are obtained in all cases. However, it should be noted that there is no correlation between the relative variations in flows or volumes of vascular territories

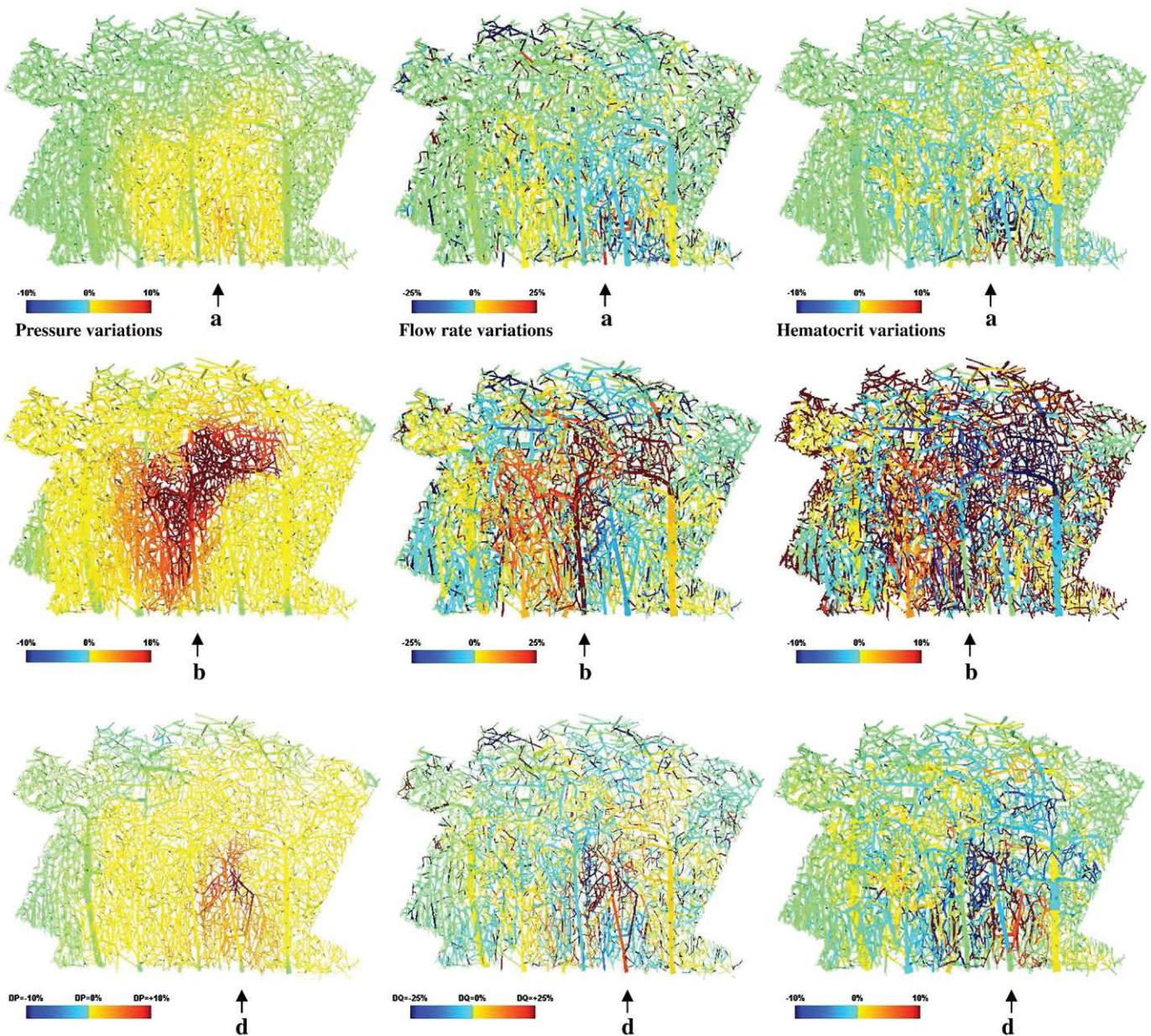


Fig. 5. Spatial distributions of pressure variations (first column), flow rate variations (second column) and hematocrit variations (third column) calculated for the local vasodilation ( $f_{vaso}=2$ ) of three different arterioles (a, b, d, indicated by arrows), relative to baseline ( $H^{in}=0.4$ ). Same conventions as in Fig. 4. Note that the baseline arterial territories of the first two vasodilated arterioles (a and b) are displayed in Part I, Fig. 5. The normalized distributions corresponding to these maps are displayed in Fig. SM13.



and their baseline values (see Fig. SM6 and SM7, Supplementary Material).

Second, a correlation between flow in parallelepiped ROIs before and after vasodilation was sought (see Fig. SM8, Supplementary Material). In both cases, strong correlations are obtained for 250  $\mu\text{m}$  ROIs ( $r=0.97$  and  $r=0.89$ , in Case 1 and Case 2, respectively), with high significance levels ( $p<0.001$ ). However, it should be noted that there is no correlation between the relative variations in ROIs flows and their baseline values (see Fig. SM9, Supplementary Material). In addition, there is no correlation between the relative variations in ROIs flows and the relative variation of the proportion of vascular space occupied by non-capillary vessels (see Fig. SM10, Supplementary Material).

#### Hemodynamic variations induced by localized arteriolar vasodilations

In order to study the variations induced by localized vasodilations, calculations have been repeated by vasodilating a different arteriolar tree each time, using boundary condition Case1. In order to give a qualitative idea of the results, we will first present representative spatial distributions of the variations of hemodynamic parameters relative to baseline, and the corresponding quantities averaged over parallelepiped ROIs. Then, in order to gain a quantitative insight on

the spatial dynamics of the hemodynamic changes, we will focus on the variations in the main arteriolar and venular trunks.

#### Characteristic spatial patterns

Fig. 5 displays the maps of pressure, flow rate and hematocrit variations relative to baseline when three different arteriolar trees are vasodilated ( $f_{\text{vaso}}=2$ ). First, pressure variations are extremely variable in spatial extent and intensity, depending on the vasodilated tree. Arterioles that exhibit a baseline vascular territory restricted to the superficial layer of the cortex (e.g., arteriole **a**, see part I) typically induce pressure variations - which are always positive - in areas less extended than arterioles whose baseline vascular territory spans the entire depth of the cortex (e.g., arterioles **b** and **d**). Unlike the pressure variations, whose intensity varies in a smooth fashion in space, the flow rate and hematocrit variations display large spatial heterogeneities. With regard to hematocrit variations, the heterogeneities do not seem to exhibit any general tendencies. With regard to flow rate variations, the vasodilated arteriolar tree systematically shows an increase in flow rate which propagates downstream. However, in general, areas of reduced flow are surrounding the areas of increased flow. These patterns of flow variations are conserved, although

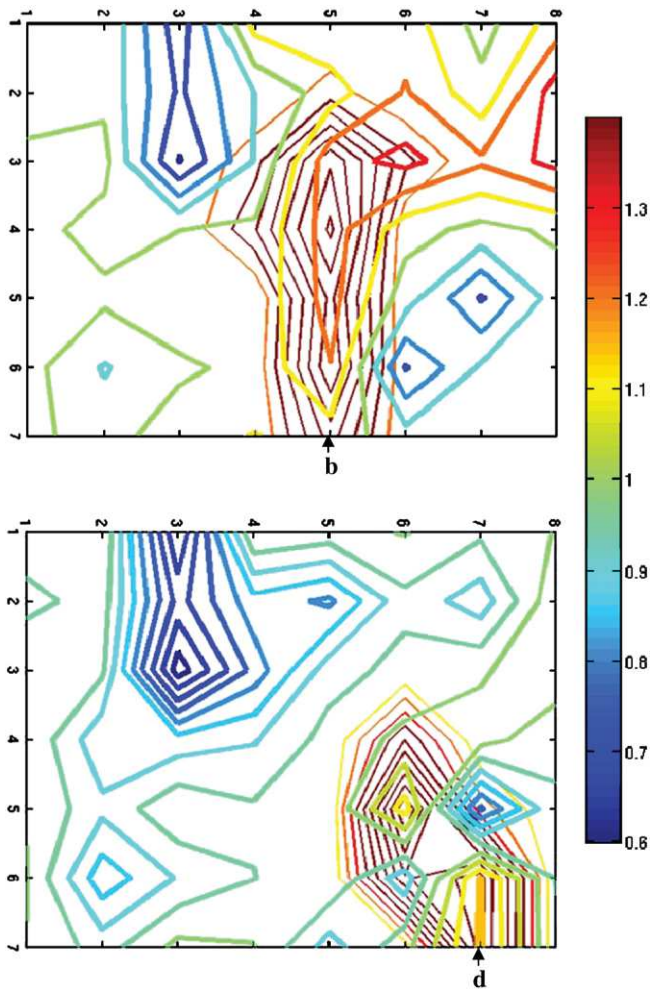


**Fig. 6.** Isocontours of the variations in ROIs vascular volume (thin lines) and ROIs flow rate (thick lines) relative to baseline when arterial trunks **b** (top) or **d** (bottom) are vasodilated. The ROIs containing the vasodilated arteries are indicated by arrows. Note that even if the local maxima of flow rate variations are situated in voxels exhibiting volume increases (i.e., voxels superimposed to the vasodilated tree), the peaks of volume and flow increase are not necessarily matched, which is obvious in the top panel. Moreover, voxels exhibiting volume increases can also display flow rate reductions. Finally, areas of flow increase are surrounded by areas of flow reduction. The size of the ROIs is 250  $\mu\text{m}$ .

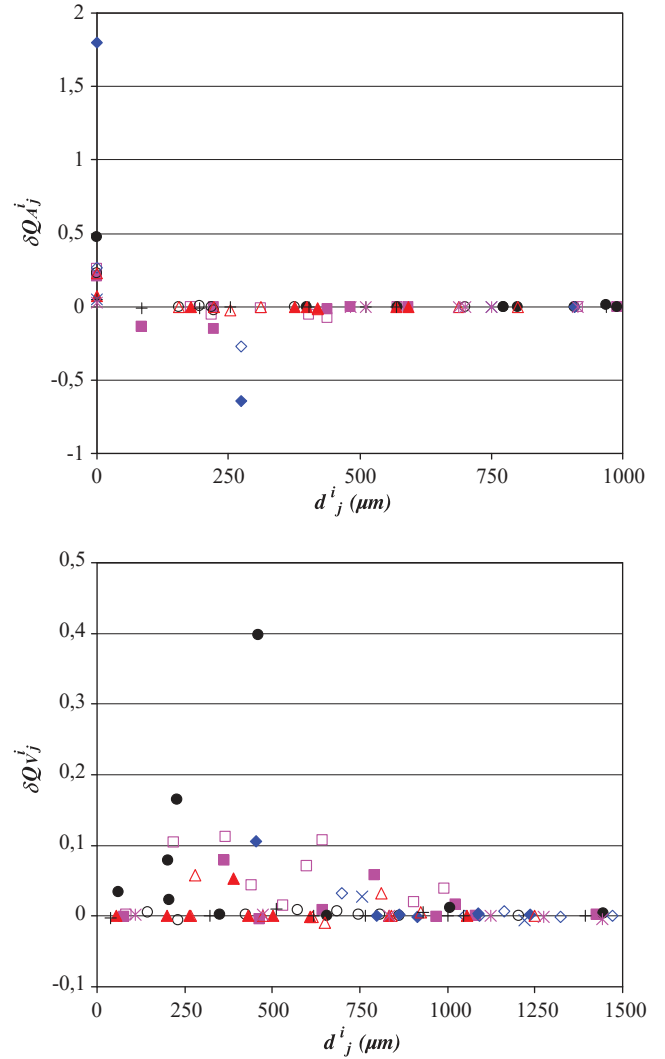


**Fig. 7.** Flow rate variations in each main arteriolar (top) or venular (bottom) trunk ( $j$ ) induced by the localized vasodilation of a given arteriolar trunk ( $i$ ), relative to baseline, as a function of the distance between  $i$  and  $j$  projected over the sulcus. The results obtained by “vasodilating” a different trunk each time are superimposed on the same graphs, using a different symbol for each calculation.

smoothed, when the variations of the flow rate averaged over 250  $\mu\text{m}$  parallelepiped ROIs are considered (see Fig. 6). Note that even if the local maxima of flow rate variations are situated in voxels exhibiting volume increases (i.e., voxels superimposed to the vasodilated tree), the peaks of volume and flow augmentation do not necessarily match. Moreover, voxels exhibiting volume augmentations can also display flow rate reductions. Finally, areas of flow augmentation are surrounded by areas of flow reduction.

#### Spatial dynamics of the flow changes

In order to clarify the qualitative tendencies described above and to extract quantitative information, the flow rate variations in each main arteriolar or venular trunk relative to baseline are plotted as a function of their distance to the vasodilated artery projected over the sulcus (Fig. 7). Even though there is a high dispersion in the magnitude of the variations, a different spatial pattern for the response of arteries and veins emerges: in the case of arteries (Fig. 7, top), the maximal variation always occurs in the vasodilated trunk ( $d_j^i = 0$ ). Then, in the immediate vicinity of the vasodilated artery, and for distances up to  $\sim 300 \mu\text{m}$ , the flow rate either exhibits no variation or a flow decrease, which demonstrates vascular steal. Further away from the vasodilated artery,

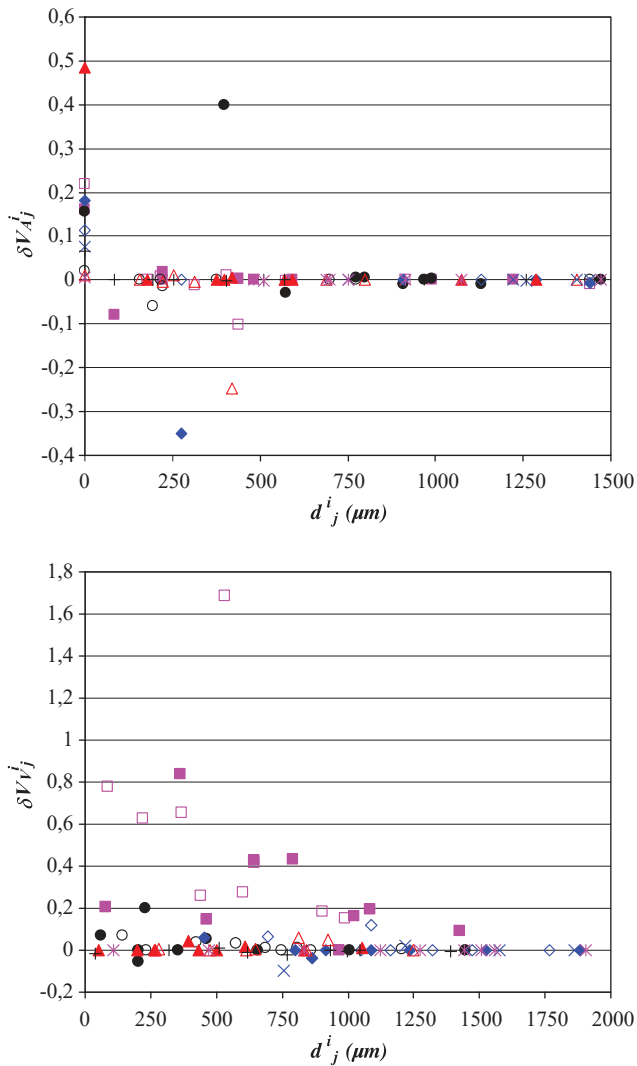


**Fig. 8.** Variation in the volume of arteriolar territories (top) or venular territories (bottom) ( $j$ ) induced by the localized vasodilation of a given arteriolar trunk ( $i$ ), relative to baseline, as a function of the distance between  $i$  and  $j$  projected over the sulcus. The results obtained by “vasodilating” a different trunk each time are superimposed on the same graphs, using a different symbol for each calculation.

the remaining arteriolar trunks are no longer influenced by this local vasodilation. In the case of veins (Fig. 7, bottom), the distance above which the influence of the vasodilation vanishes is much greater—about 1 mm. Below this distance, a peak in positive venous flow perturbation is to be observed in the range 250–500  $\mu\text{m}$ , with small perturbations in the immediate vicinity of the vasodilated artery. The variations in the volume of the territories fed by each main arteriolar trunk and in the volume of the territories drained by each venular trunk are displayed in Fig. 8. While presenting a larger dispersion, they exhibit the same general tendencies, with greater ranges of influence ( $\sim 600 \mu\text{m}$  in the case of arteries and  $\sim 1.4 \text{ mm}$  in the case of veins).

Finally, with regard to the dispersion of the magnitude of these flow rate and volume variations, it is noteworthy that, while the flow rate in the vasodilated arteriolar trunk is correlated ( $r > 0.98$ ,  $p = 0.01$ ) to its baseline values (see Fig. SM11, Supplementary Material), there is no correlation between its relative variations and baseline values (see Fig. SM11, inserts). These two results also hold as far as the volume of the territory of the vasodilated arteriolar trunk is concerned (Fig. SM11 and inserts).

## Discussion

### Main findings of the study

In this study, we simulated and analyzed the hemodynamic changes following arteriolar vasodilations either induced by global or localized activations. The main findings of this study can be summarized as follows:

- 1) Pressure, volume and flow changes induced by global vasodilations can be accurately fitted by a very simple model consisting mainly of two resistances connected in series. As a consequence, for small to moderate global vasodilations (i.e., most physiological changes, see below), the relationship between changes in volume and changes in flow is in close agreement with a power law model, the exponent of which is exactly in the range experimentally determined in previous studies,
- 2) The contribution of passive venous vasodilation is small and does not impact the simple model described above. In particular, the contribution of passive venous vasodilation to the total volume increase is small,
- 3) A weak but significant correlation between the blood flow in parallelepiped ROIs and the vascular structure in the ROIs, i.e., the proportion of vascular volume occupied by arterioles or venules, has been found. This correlation can be described by a power relationship whose exponent remains practically unchanged with respect to the baseline (no activation) exponent.
- 4) In general, following localized arteriolar vasodilations, areas of reduced flow are juxtaposed to areas of increased flow. This result still holds when blood flow is averaged over parallelepiped ROIs. In particular, localized vasodilations induce flow changes, including vascular steal, in the neighboring arteriolar trunks at short distances ( $< 300 \mu\text{m}$ ), while the distance above which the influence of this vasodilation on the neighboring veins vanishes is much greater (about 1 mm). This distance is even greater (1.4 mm) when the variations in the volume of the drained territories are considered.

Before discussing these main results and their implications for functional imaging, several methodological aspects will first be addressed. These relate mainly to:

- the parameters used to simulate global or local vasodilations, i.e., more generally blood flow control,
- and to the passive response of non-vasodilated vessels to vasodilation-induced pressure augmentations.

One of the main components involved in brain blood flow control and regulation is the smooth muscle cells associated to resistance arterioles in the pial (Girouard and Iadecola, 2006) and intra-cortical arteries (Rodríguez-Baeza et al., 1998; Girouard and Iadecola, 2006). In the human brain, the detailed electron microscopy study of corrosion casts performed by Rodríguez-Baeza et al. (1998) suggests the existence of a lower bound value for the diameter of arterioles that can exhibit active vasodilation. In order to investigate the effect of the existence of a minimal diameter in arteries exhibiting active vasodilation, two values of  $d_{\text{vaso}}$  have been chosen in the present study, the first,  $9.9\ \mu\text{m}$ , corresponding to the diameter threshold for capillary vessels and the second,  $14.9\ \mu\text{m}$ . Our calculations demonstrated that the network behavior is qualitatively independent of  $d_{\text{vaso}}$ , even though the quantitative results are influenced by its value. In dynamic conditions observed in vivo in rat brains, the magnitude of diameter increases varies from  $\sim 10\%$  to  $45\%$  (Cox et al., 1993; Woolsey et al., 1996; Hillman et al., 2007; Devor et al., 2007; Hutchinson et al., 2006). The maximal value of  $f_{\text{vaso}}$  ( $f_{\text{vaso}} = 2$  corresponding to a 100% vasodilation) used in this study has been overestimated compared to the maximal physiological increase. This overestimation permitted to reach the asymptotic behaviors of the flow patterns needed to test the goodness of fit of the simple model of resistances in series used for analyzing global vasodilations. However, due to the presence of this asymptotic regime, with saturating flow rate augmentations, the rate of increase of the regional blood flow decreases with  $f_{\text{vaso}}$ . With Boundary Condition Case 1, a 23.3% regional blood flow increase is predicted from baseline ( $f_{\text{vaso}} = 1$ ) to 50% vasodilation ( $f_{\text{vaso}} = 1.5$ ), whereas only a further 4.0% increase is predicted for a 100% vasodilation. With Boundary Condition Case 2, a 48.5% increase is predicted from baseline to 50% vasodilation whereas a further 12.8% increase is predicted for a 100% vasodilation. These orders of magnitude are consistent with the  $30.5 \pm 14.6\%$  flow rate augmentation measured by PET in response to hypercapnia in humans (Ito et al., 2003). Moreover, the orders of magnitude of flow variations predicted for the maximal value of  $f_{\text{vaso}}$  are only slightly overestimated.

Several authors have noted a significant capillary vasodilation (Villringer et al., 1994; Hutchinson et al., 2006; Vanzetta et al., 2005; Stefanovic et al., 2008). As pointed out by Stefanovic et al. (2008), in the more recent of these studies, “very little data, however, exist on the functional reactivity of capillaries.” Using two-photon laser scanning microscopy, these authors estimated the contribution of the capillaries to the total stimulation-induced CBV changes and concluded that less than  $1/5$  ( $\sim 18\%$ ) of the total blood volume increase is occurring on the level of capillaries. The remaining  $4/5$  ( $\sim 82\%$ ) corresponds to the contribution of larger vessels. Moreover, it is at present not clear whether the observed capillary dilatation is a passive consequence of arteriolar dilation or a result of an active regulation of the capillary diameter by pericytes (Peppiatt et al., 2006; Girouard and Iadecola, 2006; Fernández-Klett, 2008). Therefore, in the present study, as a reasonable first approximation, we neglected the volume increase occurring at the level of capillaries with respect to the arteriolar or venular, active or passive, vasodilation.

Regarding venules, the generally accepted opinion is that they passively inflate in response to arteriolar vasodilation as a result of their high compliance. However, as noted by Boas et al. (2008) it is not clear whether dominant volume changes occur on the arteriole side (Hillman et al., 2007; Kim et al., 2007; Lee et al., 2001; Vanzetta et al., 2005) or venous side (Buxton et al., 1998; Kong et al., 2004; Mandeville et al., 1999). Our results indicate that the arteriolar blood volume change comprises more than 96%, i.e., the major portion of the blood volume change. This result is in accordance with the results obtained by Boas et al. (2008). Moreover, the relatively insignificant contribution of venous dilation has been recently observed experimentally (Hillman et al., 2007; Kim et al., 2007; Lee et al., 2001; Vanzetta et al. (2005)). As

pointed out by Vanzetta et al. (2005), these recent results are inconsistent with the important role ascribed to venous compliance in previous theoretical models of the BOLD signal - e.g., the “balloon model” (Buxton and Frank, 1997; Buxton et al., 1998) and windkessel models (Kong et al., 2004; Mandeville et al., 1999). However, this contradiction might only be apparent. In fact, Zheng et al. (2010) recently highlighted that “these simplistic models of neurovascular coupling are not directly validated by experimental data” but are rather derived in an ad hoc fashion to reproduce the experimentally known temporal dynamics of the BOLD signal. Our results suggest that the anatomical structures corresponding to the dilation component of the vascular network would rather be arteriolar vessels, even if further work is needed to study the contribution of capillary vessels (Turner and Thomas, 2006). As already pointed out by Boas et al. (2008), this results in a strong localization of the blood volume response in the active arterioles, whereas the blood flow response is uniform across arterioles, capillaries, and venules. This would explain why new techniques as “vascular space occupancy” (VASO), which have been put forward as being non-invasively sensitive to blood volume changes have potential for greater spatial specificity at a comparable functional contrast to noise ratio as BOLD contrast techniques (see Bandettini, 2007 and references therein).

#### *Hemodynamic variations induced by global vasodilations*

Studying global vasodilations can provide information to help separate the vascular component of the signal from other components directly related to brain activity (Thomason et al., 2005). This same idea is used in functional neuroimaging when hypercapnia is used to induce an isometabolic global increase in cerebral blood flow (Rostrup et al., 2000), in order to provide a calibration reference for fMRI studies (Davis et al., 1998; Ances et al., 2008). Although this calibrated BOLD approach potentially provides a powerful tool for investigating the coupling of blood flow and oxygen metabolism both in different brain structures and in different disease states (Leontiev and Buxton, 2007), various studies have emphasized ambiguities and systematic bias (Chiarelli et al., 2007a; Ances et al., 2008) which may limit the ability to measure quantitative neurophysiological parameters underlying the fMRI signal. Estimates of CMRO<sub>2</sub> changes rely on the Davis model, a simple but non-linear model for the BOLD signal, from which the coupling of changes in CBF and CMRO<sub>2</sub> can be calculated for a functional activation paradigm. Among the parameters of the Davis model is the Grubb exponent  $\phi$ , which models the linear relationship on a logarithmic scale found between cerebral blood flow (CBF) and cerebral blood volume (CBV).

While this relationship between CBV and CBF has been widely studied experimentally (Leung et al., 2009), only few studies have intended to investigate the theoretical basis of this relationship, under CO<sub>2</sub> manipulation. To address this, several simplified vascular models have been considered by Piechnik et al. (2008). To our knowledge, the present study is the first one to be performed on a real micro-vascular cortical network of the human brain. First, it is worthwhile noting that the pressure and flow changes induced by vascular reactivity can be accurately analysed using a simple model involving two resistances in series (Eqs. (4) to (8)) somewhat similar to the M2 model proposed by Piechnik et al. (2008). Of course, the resistance values and corresponding volumes derived from our real anatomical vascular model will vary depending on the macroscopic architectural properties, for example the vascular densities, of the vascular network of the brain area under study. Second, from these values, quantitative estimates of the Grubb exponent  $\phi$  can be obtained from Eq. (10). As indicated in the Results section, the value obtained in this way is between 0.16 (Case 2) and 0.30 (Case 1), which is in close accordance with the range 0.18–0.36 determined by several groups using recent techniques such as laser Doppler flowmetry and optical imaging in brain activation studies (Mandeville et al., 1999; Jones et al., 2001;

Sheth et al., 2004a and references therein, Leung et al., 2009; Boas and Payne, 2009). This is a remarkable result because:

- 1/ the theoretical range is very robust, its lower and upper limit being determined by the Boundary Condition prescribed on interrupted capillary segments, i.e., the type of interactions between the territory under study and the neighboring territories. In particular, this range is not affected by the various assumptions tested in our study, with both minor influence of the minimal diameter of arteries exhibiting active vasodilation ( $d_{vaso}$ ), see Table 2, and of the passive vasodilation of venules, see Table 4.
- 2/ no adjustable parameters was used to artificially match this experimental range.

On the contrary, in the three-compartmental model of Piechnik et al. (2008), the value of  $\phi$  can be adjusted by modifying the resistance and volume contribution of the regulating vascular bed to the total resistance and volume.<sup>1</sup> For example, with realistic values of these contributions, a range 0.05–0.47 is obtained, with the worst prediction ( $\phi=0.05$ ) corresponding to “the archetypal assumption that the regulating bed has very little volume (10% of total volume).” From this result, these authors conclude that “parts of the capillary and/or venous bed must also take part in vasoreactive responses.” This is in contradiction with the present results: with the complex vascular structure considered, the volume fraction of the reactive bed, given by  $\frac{V_0}{V_0 + V_\infty}$ , is between 15% and 7%, depending on the minimal diameter of arteries exhibiting active vasodilation ( $d_{vaso}$ ). The resistive contribution of the reactive bed ( $\frac{R_0}{R_0 + R_\infty}$ ) is between 11% and 45%. Thus, due to the complexity of the vascular structure under study, the broad presumption that the regulating bed is responsible for most of the resistance, is not valid, either. As a conclusion, the approach presented here could provide a theoretical framework for analyzing the variations of  $\phi$  among various brain areas of different architectural characteristics, in steady state conditions. Further methodological developments will however be needed to handle transient states in order to investigate the time dependence of  $\phi$  during neuronal activation (Kong et al., 2004; Zheng and Mayhew, 2009).

Although a simple model involving two resistances in series can accurately describe the hemodynamic variations induced by global vasodilations at network scale, this model cannot account for the heterogeneities we have evidenced throughout the network. However, architectural heterogeneity (e.g., vascular density variations in both directions parallel and orthogonal to the cortical depth, irregular blobs, etc.) is a major feature of the human intra-cortical vascular architecture as pointed out by Lauwers et al. (2008). Heterogeneity of hemodynamic variables (hematocrit, blood velocity, transit time) also constitutes a fundamental characteristic of intra-cortical microcirculation (Pawlik et al., 1981; Kuschinsky and Paulson, 1992; Villringer et al., 1994). Thus, it is not surprising to observe a large spectrum of variations in response to prescribed global arteriolar vasodilations. Actually, such heterogeneities in the spatiotemporal characteristics of cerebral blood volume (CBV) and flow (CBF) responses have also been observed between different areas (Wu et al., 2002; Chiarelli et al., 2007b; Tuunanen and Kauppinen, 2006; Tuunanen et al. 2006; Vafaee and Gjedde, 2004), or even within the same cortical region (Kida et al., 2007; Jin and Kim, 2008). Several authors (Bandettini, 2007; Muller et al., 2005; Formisano and Goebel, 2003) have noted that the sources

<sup>1</sup> To be precise, in the three-compartmental model (M2) of Piechnik et al., (2008) the curve (CBV/CBV<sub>0</sub>) as a function of (CBF/CBF<sub>0</sub>) can be adequately described as a straight line within physiologically practical limits. Therefore, all results are given in the form of the slope of this straight line, and not as the exponent of a power law. However, for small flow rate variations (i.e., when CBF/CBF<sub>0</sub> = (1 + ε), ε being a small parameter), the first order of the series expansion of the power law CBV/CBV<sub>0</sub> = (1 + ε)<sup>φ</sup> is CBV/CBV<sub>0</sub> = 1 + φε. Thus, it is possible to directly compare our results with the results of Piechnik et al. Note that in both cases, no conclusions can be drawn on the curvature of the relationship between CBV and CBF.

of this variability across the brain are likely dominated by variations in the vasculature rather than underlying neuronal activity. This is consistent with our results simulating an isometabolic increase in blood flow. In addition, our results demonstrate that hemodynamic parameters, and in particular cerebral blood flow, do not only vary across subject populations, individuals, and regions in the brain but also across voxels and even within voxels. This hemodynamic variability poses a limit on how fMRI can be used (Bandettini, 2009) leading an author as well-known as Logothetis to go further and suggest that “the magnitude of the fMRI signal cannot be quantified to reflect accurately differences between brain regions, or between tasks within the same region” (Logothetis, 2008). Moreover, the absence of correlation between the relative variations of flow or volume of the vascular territories and their baseline values, whereas their absolute values following vasodilation do correlate with their baseline values, can be interpreted as a non-linear behavior. Though it may be difficult to separate non-linear neuronal effects from vascular response nonlinearities, a recent study showed that hemodynamic nonlinearities do affect BOLD fMRI response timing and magnitude, and that, “if not properly taken into account such vascular nonlinearities confound the interpretation of underlying neuronal events” (de Zwart et al., 2009). Moreover, the fact that the absolute changes in blood flow, rather than the normalized (percent) changes, are most closely coupled to neural activity across normal and hypercapnic conditions (Huppert et al., 2009) might be at least partially interpreted through the biomechanical mechanisms pointed out in the present study.

#### *Hemodynamic variations induced by local vasodilations*

Due to the indirect nature of the BOLD signal as a surrogate for neural activity, the spatial resolution of BOLD fMRI is a complex interplay between technical constraints (e.g., field strength, see Harel et al., 2006) that determine voxel size, physics (e.g., signal production as a function of sequence type and sensitivity to various vessel types and sizes, see Uludağ et al., 2009) and vascular point spread function (Menon and Goodyear, 1999; Sheth et al., 2004b; Harel et al., 2006; Shmuel et al., 2007; Yacoub et al., 2008; Kim and Fukuda, 2008). Thus, as pointed out by Harrison et al., 2002, further detailed mapping studies of blood pathways and associated control points are needed to estimate the ultimate spatial resolution of hemodynamic-based functional imaging methods such as fMRI. However, experimental techniques enabling to perform such mapping studies, such as two-photon laser microscopy, are restricted to small fields of view (between 180 × 180 μm<sup>2</sup> and 400 × 400 μm<sup>2</sup>, Hillman et al., 2007; Hutchinson et al., 2006; Nishimura et al., 2007; Chaigneau et al., 2003), typically smaller or of the same order as voxel size in fMRI. Fluid dynamic modeling is a powerful alternative tool for studying blood flow reorganizations at larger scale. In particular, the spatial extent (point spread function) of the hemodynamic changes induced by localized arteriolar vasodilations, which are assumed to be representative of a local increase in metabolic demand, has been investigated. We have shown that a localized vasodilation induces flow changes, including vascular steal (see below), in the neighboring arteriolar trunks at small distances (<300 μm), while the distance above which the influence of this vasodilation on the neighboring veins vanishes is much greater (about 1 mm), see Fig. 7. Moreover, with regard to changes in the volumes of vascular territories fed or drained by an arteriole or a venule, respectively, as a function of their distance to the vasodilated artery (Fig. 8), the range of influence is even greater (~600 μm in the case of arteries and ~1.4 mm in the case of veins). Consistent with the spatial scales described above, the point spread function (PSF) of the CBF response to visual stimulation has been measured to be ~0.5 mm in the cat primary visual cortex by arterial spin labeling fMRI at 9.4 T, whereas a larger value (~1.6 mm) has been obtained by BOLD fMRI using a conventional GE-EPI sequence (Park et al., 2004). In fact, it is recognized that GE-EPI is

sensitive to local susceptibility gradients (Ogawa et al., 1992) which originate predominantly near veins (Uludağ et al., 2009). Note that, as underlined by many authors (Harrison et al., 2002; Harel et al., 2006; Weber et al., 2008), the vascular PSF is closely linked to the minimum spatial scale for the vascular control of blood flow changes. In this context, our results demonstrate that the regulation of blood flow at the level of individual intra-cortical arterioles, without any active or passive modifications of vessel diameter at capillary level, is sufficient to explain the submillimeter PSF experimentally measured by ASL fMRI at 9.4 T. Moreover, our results theoretically confirm the need to develop sequences yielding high micro-vasculature weighting of the fMRI signal, excluding the contribution of intra-cortical veins, especially in the context of ultra-high magnetic fields (Yacoub et al., 2008).

A specific aspect of BOLD contrast where there is continuing controversy on the interpretation of fMRI data is the existence of negative BOLD and its link with neural activity (Harel et al., 2002; Shmuel et al., 2002; Devor et al., 2007; Northoff et al., 2007; Schridde et al., 2008; Woolsey et al., 1996). In the first paper of this series, Woolsey et al. (1996) studied the links between neuronal units and micro-vascular modules in cerebral cortex of the rodent whisker-barrel system. They showed that activation that increased flow to particular barrels often led to reduced flow to the adjacent cortex. With the continuous improvements in spatial resolution in the context of ultra-high field imaging, the negative BOLD effect is being experimentally observed in fMRI studies at 7T (Kennerley et al., 2007). In order to address this controversy, Boas et al. (2008) used their vascular anatomical network (VAN) model to perform a simulation study of the hemodynamic spatiotemporal response to brain activation. They predicted a passive surround negative vascular response, with a surround decrease in blood flow representing ~15% of the center increase. The corresponding surround decrease in oxygenated hemoglobin represented less than 5% of its center increase, lower than the value of ~18% recently measured in the rat following somatosensory stimulation (Devor et al., 2007). Thus, these authors concluded that either additional active surround vasoconstriction is required to explain the experimental data, or the insufficient complexity of the VAN model architecture, which does not fully represent the three dimensional asymmetric structure of a branched vascular network, may explain this discrepancy. Our results are in accordance with this last hypothesis. Indeed, at the arterial trunk level (see Fig. 7, top), the ratio between maximal surround decrease in flow and maximal center increase (i.e., flow increase in the vasodilated arterial trunk) is  $23 \pm 29\%$  (mean  $\pm$  SD), with a minimal value of 0% (no surround negativity) and a maximal value of 102% (surround decrease greater than center increase). Even at the voxel scale (see Fig. 6), relative flow increases (compared to baseline) are of order 15–30% whereas relative flow decreases are of order 40%, i.e., more than the center increase. However, as quantitative experimental data on surround vs. center flow response are lacking, further investigation is needed to confirm whether negative signal change in zones surrounding an activated area is a purely passive hemodynamic “stealing” effect or if it is also induced by additional surround vasoconstriction and neuronal inhibition. In particular, in our model, the effect of limit conditions at interrupted capillary segments, which has been investigated in detail (see part I) with regard to baseline flow, could impact the hemodynamic response to local vasodilations. Thus, it is important to interpret the present results with caution until further studies on thicker sections of human brain can be performed. In fact, the widespread view (Iadecola and Nedergaard, 2007) rejects the existence of this stealing effect. As clearly pointed out by Faraci and Heistad (1990), this view means that an upstream regulation mechanism acting at the level of pial arteries suppresses the stealing effect that would otherwise occur, as confirmed in the present paper, if the vasodilatation was restricted to localized cortical arterioles. However, upstream regulation (Segal et al., 1989) would inevitably

broaden the area where stimulation-induced flow changes occur. This would in turn degrade the point spread function. Further investigation, including pial vessels in the network, is then needed to simulate the effects of such an upstream regulation.

With regard to the above controversy, the issue of spatial resolution is of critical importance, and could even explain the diverging results about the occurrence of vascular steal in normal physiologic conditions: smoothing effects of fMRI, particularly at lower fields, mask very localized negative flow changes. In particular, our results suggest that for voxel sizes above 1 mm, corresponding to twice the range of influence of arterioles over neighboring arterioles, no steal can be detected. This corresponds to the typical spatial resolution at lower fields. In the context of ultra-high field fMRI, however, where the voxel size reaches ~500  $\mu\text{m}$  (Yacoub et al., 2007, 2008), the experimental observation of an eventual steal will depend on the relative position between the active arteriole and the voxel center. Therefore, with such a spatial resolution, vascular steal may or may not be observed. Smaller voxel sizes will be needed to conclude on the experimental reality of this stealing phenomenon in fMRI.

#### *Future directions*

We have presented the first simulation study of brain blood flow regulation by intra-cortical arterioles in an anatomically accurate large human vascular network. We have shown that such simulations can be useful to analyze the hemodynamic component of brain activation studies. This hemodynamic component, and more specifically the relationship between the micro-vascular architectural characteristics and the BOLD signal, has been the subject of only a limited number of papers (Ogawa et al., 1993; Boxerman et al., 1995; Hoogenraad et al., 2001; Uludağ et al., 2009) compared to the tremendous amount of work focused on neuronal metabolism and cerebro-vascular coupling. Moreover, in these latter papers, the micro-vascular architectural and hemodynamic heterogeneity has not been taken into account for studying the BOLD signal dependence on cerebral blood flow and oxygen consumption. For example, theoretical models of BOLD signal production (Yablonskyi and Haacke, 1994; Kiselev and Posse, 1999) assume random distributions of infinite paramagnetic cylinders in order to represent the micro-vascular architecture. This simplification is partly due to the lack of morphometric and topological data about human brain micro-vascular networks and partly due to the complexity of the description of the transverse magnetization temporal evolution at the microscopic level, which involves tracking the trajectories of a large number of individual protons during their transport by diffusion and convection (Lagrangian approach). We believe that this last difficulty could be overcome by using an alternative Eulerian approach, where the modified Bloch equation (Gao and Gore, 1991) is solved on a fixed mesh. Such an approach has previously been used with success to study flow related artifacts in an anatomically realistic stenotic carotid bifurcation in the context of magnetic resonance angiography (Lorthois et al., 2005). For that purpose, the methodology presented in the companion paper for blood flow simulation (Lorthois et al., *Neuroimage*, 2011) should first be coupled to a model of oxygen transport. Such a model, using a boundary integral method that does not require the spatial discretization of the tissue volume, has been used for modeling oxygen transfers from any 3-dimensional network supplying a finite region of tissue (Secomb et al., 2004). This would also enable the quantitative study of the variations in oxygen extraction induced by the slower increase of erythrocyte mean transit time compared to blood mean transit time following global vasodilations, i.e., in isometabolic conditions. To our knowledge, such variations have not been taken into account in previous theoretical models of the BOLD signal. In these models, variations in oxygen extraction are explicitly linked to the flow rate by a relationship

analogous to the well-known model of Renkin-Crone (Renkin, 1959; Crone, 1963). Neuro-vascular coupling (i.e., the link between neuronal activation and changes in flow) are schematically modeled either by directly prescribing the temporal dynamics of the flow entering the system (Buxton et al., 1998; Aubert and Costalat, 2002; Valabrègue et al., 2003) or by prescribing an ad hoc non-linear relationship between the time-course of the imposed stimulus and the inlet flow (Zheng et al., 2002; Buxton et al., 2004).

Of course, the results presented in this paper are restricted to a single cortical area (secondary visual cortex) of a single human brain (a 60 year old female who died from an abdominal lymphoma with no known vascular or cerebral disease). Further work on various cortical areas and various conditions is necessary in order to perform parametric studies of the effect of vascular architecture (in particular vascular density) on the flow reorganizations induced by arteriolar vasodilations in the context of functional neuroimaging. In this context, it may also prove useful to perform numerical studies on structures generated *in silico* to reproduce the main known morphometric and topological characteristics of the human intra-cortical networks (Cassot et al., 2006; Lauwers et al., 2008; Cassot et al., 2010; Lorthois and Cassot, 2010). Such studies could either use ad hoc algorithms to reproduce the fractal properties of arteriolar and venular trees (Schreiner et al., 2005; Bui et al., 2009) or be based on morphogenesis models (Nguyen et al., 2006; Lorthois and Cassot, 2010).

Even though the present study is restricted to a single cortical area, the hemodynamic component of various functional neuroimaging techniques has nevertheless been isolated, for the first time, from metabolic and neuronal components. A direct relationship between this hemodynamic component and several known characteristics of the BOLD signal has been demonstrated. This first set of results will allow future comparisons with the hemodynamic behavior of other brain areas with different vascular density (e.g., primary visual cortex) or pathologic networks.

Supplementary materials related to this article can be found online at doi:10.1016/j.neuroimage.2010.10.040.

## Acknowledgments

Kamil Uludağ must be thanked for useful discussions. We gratefully acknowledge the anonymous referees for their constructive comments and suggestions. We also thank Victoria McBride who considerably helped to improve the English of this manuscript. This work has been partly supported by ACITechnologies pour la Santé Grant Number 02TS031 of the French Department of Education, Research and Technology and by GDR CNRS 2760 "Biomécanique des fluides et des transferts: Interactions Fluide Structure Biologique".

## References

Ances, B.M., Leontiev, O., Perthen, J.E., Liang, C., Lansing, A.E., Buxton, R.B., 2008. Regional differences in the coupling of cerebral blood flow and oxygen metabolism changes in response to activation: implications for BOLD-fMRI. *Neuroimage* 39, 1510–1521.

Aubert, A., Costalat, R., 2002. A model of the coupling between brain electrical activity, metabolism, and hemodynamics: application to the interpretation of functional neuroimaging. *Neuroimage* 17, 1162–1181.

Bandettini, P., 2007. Functional MRI today. *Int. J. Psychophysiol.* 63, 138–145.

Bandettini, P., 2009. What's new in neuroimaging methods? *Ann. NY Acad. Sci.* 1156, 260–293.

Boas, D., Payne, S., 2009. Comment on 'Estimating a modified Grubb's exponent in healthy human brains with near infrared spectroscopy and transcranial Doppler'. *Physiol. Meas.* 30, L9–L11.

Boas, D.A., Jones, S.R., Devor, A., Huppert, T.J., Dale, A.M., 2008. A vascular anatomical network model of the spatio-temporal response to brain activation. *Neuroimage* 40, 1116–1129.

Boxerman, J.L., Hamberg, L.M., Rosen, B.R., Weisskoff, R.M., 1995. MR contrast due to intravascular magnetic susceptibility perturbations. *Magn. Reson. Med.* 34, 555–566.

Bui, A., Satalo, I.D., Manasseh, R., Liffman, K., 2009. Dynamics of pulsatile flow in fractal models of vascular branching networks. *Med. Biol. Eng. Comput.* 47, 763–772.

Buxton, R.B., Frank, L.R., 1997. A model for the coupling between cerebral blood flow and oxygen metabolism during neural stimulation. *J. Cereb. Blood Flow Metab.* 17, 64–72.

Buxton, R.B., Wong, E.C., Frank, L.R., 1998. Dynamics of blood flow and oxygenation changes during brain activation: the Balloon model. *Magn. Reson. Med.* 39, 855–864.

Buxton, R.B., Uludağ, K., Dubowitz, D.J., Liu, T.T., 2004. Modeling the hemodynamic response to brain activation. *Neuroimage* 23, S220–S233.

Cassot, F., Lauwers, F., Fouard, C., Prohaska, S., Lauwers-Cances, V., 2006. A novel three-dimensional computer-assisted method for a quantitative study of microvascular networks of the human cerebral cortex. *Microcirculation* 13, 1–18.

Cassot, F., Lauwers, F., Lorthois, S., Puwanarajah, P., Cances-Lauwers, V., Duvernoy, H., 2010. Branching patterns for arterioles and venules of the human cerebral cortex. *Brain Res.* 1313, 62–78.

Chaigneau, E., Oheim, M., Audinat, E., Charpak, S., 2003. Two-photon imaging of capillary blood flow in olfactory bulb glomeruli. *Proc. Natl. Acad. Sci. USA* 100, 13081–13086.

Chiarelli, P.A., Bulte, D.P., Piechnik, S., Jezzard, P., 2007a. Sources of systematic bias in hypercapnia-calibrated functional MRI estimation of oxygen metabolism. *Neuroimage* 34, 35–43.

Chiarelli, P.A., Bulte, D.P., Gallichan, D., Piechnik, S.K., Wise, R., Jezzard, P., 2007b. Flow-metabolism coupling in human visual, motor, and supplementary motor areas assessed by magnetic resonance imaging. *Magn. Reson. Med.* 57, 538–547.

Chien, S., Usami, S., Skalak, R., 1984. Blood flow in small tubes. In: Geiger, S.R. (Ed.), *Handbook of physiology, section 2: the cardiovascular system, volume IV, part I.* American Physiological Society, Bethesda, Md, pp. 217–249.

Cox, S.B., Woolsey, T.A., Rovainen, C.M., 1993. Localized dynamic changes in cortical blood flow with whisker stimulation corresponds to matched vascular and neuronal architecture of rat barrels. *J. Cereb. Blood Flow Metab.* 13, 899–913.

Crone, C., 1963. The permeability of capillaries in various organs as determined by use of the 'indicator diffusion' method. *Acta Physiol. Scand.* 58, 292–305.

Davis, T.L., Kwong, K.K., Weisskoff, R.M., Rosen, B.R., 1998. Calibrated functional MRI: mapping the dynamics of oxidative metabolism. *Proc. Natl. Acad. Sci. USA* 95, 1834–1839.

de Zwart, J., van Gelderen, P., Jansma, M., Fukunaga, M., Bianciardi, M., Duyn, J., 2009. Hemodynamic nonlinearities affect BOLD fMRI response timing and amplitude. *Neuroimage* 47, 1649–1658.

D'Esposito, M., Deouell, L.Y., Gazzaley, A., 2003. Alterations in the BOLD fMRI signal with ageing and disease: a challenge for neuroimaging. *Nat. Rev. Neurosci.* 4, 863–872.

Devor, A., Tian, P., Nishimura, N., Teng, I.C., Hillman, E.M., Narayanan, S.N., Ulbert, I., Boas, D.A., Kleinfeld, D., Dale, A.M., 2007. Suppressed neuronal activity and concurrent arteriolar vasoconstriction may explain negative blood oxygenation level-dependent signal. *J. Neurosci.* 27, 4452–4459.

Duong, T.Q., Kim, D.S., Ugurbil, K., Kim, S.G., 2001. Localized cerebral blood flow response at submillimeter columnar resolution. *Proc. Natl. Acad. Sci. USA* 98, 10904–10909.

Faraci, F.M., Heistad, H.H., 1990. Regulation of large cerebral arteries and cerebral microvascular pressure. *Circ. Res.* 66, 8–17.

Fernández-Klett, F., 2008. Active constriction of brain capillaries in vitro and in vivo. *J. Vasc. Res.* 45 (S2), 66 (A).

Formisano, E., Goebel, R., 2003. Tracking cognitive processes with functional MRI mental chronometry. *Curr. Opin. Neurobiol.* 13, 174–181.

Gao, J.H., Gore, J.C., 1991. A numerical investigation of the dependence of NMR signal from pulsatile blood flow in CINE pulse sequences. *Med. Phys.* 18, 342–349.

Girouard, H., Iadecola, C., 2006. Neurovascular coupling in the normal brain and in hypertension, stroke, and Alzheimer disease. *J. Appl. Physiol.* 100, 328–335.

Grubb, R.L., Raichle, M.E., Eichling, J.O., Ter-Pogossian, M.M., 1974. The effects of changes in PaCO<sub>2</sub> cerebral blood volume, blood flow, and vascular mean transit time. *Stroke* 5, 630–639.

Harel, N., Lee, S.P., Nagaoka, T., Kim, D.S., Kim, S.G., 2002. Origin of negative blood oxygenation level-dependent fMRI signals. *J. Cereb. Blood Flow Metab.* 22, 908–917.

Harel, N., Ugurbil, K., Uludağ, K., Yacoub, E., 2006. Frontiers of brain mapping using MRI. *J. Magn. Reson. Imaging* 23, 945–957.

Harrison, R.V., Harel, N., Panesar, J., Mount, R.J., 2002. Blood capillary distribution correlates with hemodynamic-based functional imaging in cerebral cortex. *Cereb. Cortex* 12, 225–233.

Hillman, E.M.C., Devor, A., Bouchard, M.B., Dunn, A.K., Krauss, G.W., Skoch, J., Bacskai, B.J., Dale, A.M., Boas, D.A., 2007. Depth-resolved optical imaging and microscopy of vascular compartment dynamics during somatosensory stimulation. *Neuroimage* 35, 89–104.

Hoogenraad, F.G., Pouwels, P.J., Hofman, M.B., Reichenbach, J.R., Sprenger, M., Haacke, E.M., 2001. Quantitative differentiation between BOLD models in fMRI. *Magn. Reson. Med.* 45, 233–246.

Huppert, T.J., Jones, P.B., Devor, A., Dunn, A.K., Teng, I.C., Dale, A.M., Boas, D.A., 2009. Sensitivity of neural-hemodynamic coupling to alterations in cerebral blood flow during hypercapnia. *J. Biomed. Opt.* 14. doi:10.1117/1.3210779.

Hutchinson, E.B., Stefanovic, B., Koretsky, A.P., Silva, A.C., 2006. Spatial flow-volume dissociation of the cerebral microcirculatory response to mild hypercapnia. *Neuroimage* 32, 520–530.

Iadecola, C., 2004. Neurovascular regulation in the normal brain and in Alzheimer's disease. *Nat. Rev. Neurosci.* 5, 347–360.

Iadecola, C., Nedergaard, M., 2007. Glial regulation of the cerebral microvasculature. *Nat. Rev. Neurosci.* 10, 1369–1376.

Ito, H., Kanno, M., Ibaraki, M., Hatazawa, J., Miura, S., 2003. Changes in human cerebral blood flow and cerebral blood volume during hypercapnia measured by Positron Emission Tomography. *J. Cereb. Blood Flow Metab.* 23, 665–670.

Jin, T., Kim, S.G., 2008. Cortical layer-dependent dynamic blood oxygenation, cerebral blood flow and cerebral blood volume responses during visual stimulation. *Neuroimage* 43, 1–9.

- Jones, M., Berwick, J., Johnston, D., Mayhew, J., 2001. Concurrent optical imaging spectroscopy and laser Doppler flowmetry: the relationship between blood flow, oxygenation and volume in rodent barrel cortex. *Neuroimage* 13, 1002–1015.
- Kennerley, A.J., Berwick, J., Boorman, L., Zheng, Y., Mayhew, J., 2007. Investigation of the negative BOLD and CBV fMRI response to rodent whisker stimulation at 7T. Annual Meeting of the Society For Neuroscience, San Diego <http://www.spinsn.group.shef.ac.uk/spinsn/PDFs/KennerleySFN2007.pdf>.
- Kida, I., Rothman, D.L., Hyder, F., 2007. Dynamics of changes in blood flow, volume, and oxygenation: implications for dynamic functional magnetic resonance imaging calibration. *J. Cereb. Blood Flow Metab.* 27, 690–696.
- Kim, S.G., Fukuda, M., 2008. Lessons from fMRI about mapping cortical columns. *Neuroscientist* 14, 287–299.
- Kim, T., Hendrich, K.S., Masamoto, K., Kim, S.G., 2007. Arterial versus total blood volume changes during neural activity-induced cerebral blood flow change: implication for BOLD fMRI. *J. Cereb. Blood Flow Metab.* 27, 1235–1247.
- Kiselev, V.G., Posse, S., 1999. Analytical model of susceptibility-induced MR signal dephasing: effect of diffusion in a microvascular network. *Magn. Reson. Med.* 41, 499–509.
- Kong, Y., Zheng, Y., Johnston, D., Martindale, J., Jones, M., Billings, S., Mayhew, J., 2004. A model of the dynamic relationship between blood flow and volume changes during brain activation. *J. Cereb. Blood Flow Metab.* 24, 1382–1392.
- Kuschinsky, W., Paulson, O.B., 1992. Capillary circulation in the brain. *Cerebrovasc. Brain Metab. Rev.* 4, 261–286.
- Lauwers, F., Cassot, F., Lauwers-Cances, V., Puwanarajah, P., Duvernoy, H., 2008. Morphometry of the human cerebral cortex microcirculation: general characteristics and space-related profiles. *Neuroimage* 39, 936–948.
- Lee, S.P., Duong, T.Q., Yang, G., Iadecola, C., Kim, S.G., 2001. Relative changes of cerebral arterial and venous blood volumes during increased cerebral blood flow: implications for BOLD fMRI. *Magn. Reson. Med.* 45, 791–800.
- Leontiev, O., Buxton, R.B., 2007. Reproducibility of BOLD, perfusion, and CMRO2 measurements with calibrated-BOLD fMRI. *Neuroimage* 35, 175–184.
- Leung, T.S., Tachtsidis, I., Tisdall, M.M., Pritchard, C., Smith, M., Elwell, C.E., 2009. Estimating a modified Grubb's exponent in healthy human brains with near infrared spectroscopy and transcranial Doppler. *Physiol. Meas.* 30, 1–12.
- Logothetis, N.K., 2008. What we can do and what we cannot do with fMRI. *Nature* 453, 869–878.
- Logothetis, N.K., Wandell, B.A., 2004. Interpreting the BOLD signal. *Annu. Rev. Physiol.* 66, 735–769.
- Lorthois, S., Cassot, F., 2010. Fractal analysis of vascular networks: insights from morphogenesis. *J. Theor. Biol.* 262, 614–633.
- Lorthois, S., Stroud-Rossman, J., Berger, S., Jou, L.D., Saloner, D., 2005. Numerical simulation of magnetic resonance angiographies of an anatomically realistic stenotic carotid bifurcation. *Ann. Biomed. Eng.* 33, 270–283.
- Lorthois, S., Cassot, F., Lauwer, L., 2011. Simulation study of brain blood flow regulation by intra-cortical arterioles in an anatomically accurate large human vascular network. Part I. Methodology and baseline flow. *Neuroimage* 54, 1031–1042.
- Mandeville, J.B., Marota, J.J., Ayata, C., Zaharchuk, G., Moskowitz, M.A., Rosen, B.R., Weisskoff, R.M., 1999. Evidence of a cerebrovascular postarteriole windkessel with delayed compliance. *J. Cereb. Blood Flow Metab.* 19, 679–689.
- Menon, R.S., Goodyear, B.G., 1999. Submillimeter functional localization in human striate cortex using BOLD contrast at 4 Tesla: implications for the vascular point-spread function. *Magn. Reson. Med.* 41, 230–235.
- Muller, K., Neumann, J., Lohmann, G., Mildner, T., von Cramon, D.Y., 2005. The correlation between blood oxygenation level-dependent signal strength and latency. *J. Magn. Reson. Imaging* 21, 489–494.
- Nguyen, T.H., Eichmann, A., Le Noble, F., Fleury, V., 2006. Dynamics of vascular branching morphogenesis: the effect of blood and tissue flow. *Phys. Rev. E Stat. Nonlin. Soft Matter Phys.* 73, 061907.
- Nishimura, N., Schaffer, C.B., Friedman, B., Lyden, P.D., Kleinfeld, D., 2007. Penetrating arterioles are a bottleneck in the perfusion of neocortex. *Proc. Natl Acad. Sci. USA* 104, 365–370.
- Northoff, G., Walter, M., Schulte, R.F., Beck, J., Dydak, U., Henning, A., Boeker, H., Grimm, S., Boesiger, P., 2007. GABA concentrations in the human anterior cingulate cortex predict negative BOLD responses in fMRI. *Nat. Neurosci.* 10, 1515–1517.
- Ogawa, S., Tank, D.W., Menon, R., Ellerman, J.M., Kim, S.G., Merkle, H., Ugurbil, K., 1992. Intrinsic signal changes accompanying sensory stimulation: functional brain mapping with magnetic resonance imaging. *Proc. Natl. Acad. Sci. USA* 89, 5951–5955.
- Ogawa, S., Menon, R.S., Tank, D.W., Kim, S.G., Merkle, H., Ellermann, J.M., Ugurbil, K., 1993. Functional brain mapping by BOLD contrast magnetic resonance imaging: a comparison of signal characteristics with a biophysical model. *Biophys. J.* 64, 803–812.
- Park, J.C., Ronen, I., Toth, L.J., Ugurbil, K., Kim, D.S., 2004. Comparison of point spread function of BOLD and ASL fMRI at an ultra-high magnetic field, 9.4 T. *Proc. Intl. Soc. Magn. Reson. Med.* 11, 1014.
- Pawlik, G., Rackl, A., Bing, R.J., 1981. Quantitative capillary topography and blood flow in the cerebral cortex of cats: an in vivo microscopic study. *Brain Res.* 208, 35–58.
- Peppiatt, C.M., Howarth, C., Mobbs, P., Attwell, D., 2006. Bidirectional control of CNS capillary diameter by pericytes. *Nature* 443 (7112), 700–704.
- Piechnik, S.K., Chiarelli, P.A., Jezzard, P., 2008. Modeling vascular reactivity to investigate the basis of the relationship between cerebral blood volume and flow under CO2 manipulation. *Neuroimage* 39, 107–118.
- Pries, A.R., Secomb, T.W., Gaetgens, P., Gross, J.F., 1990. Blood flow in microvascular networks. Experiments and simulation. *Circ. Res.* 67, 826–834.
- Renkin, E.M., 1959. Transport of potassium-42 from blood to tissue in isolated mammalian skeletal muscles. *Am. J. Physiol.* 197, 1205–1210.
- Rodriguez-Baeza, A., Reina-de la Torre, F., Ortega-Sanchez, M., Sahuquillo-Barris, J., 1998. Perivascular structures in corrosion casts of the human central nervous system: a confocal laser scanning electron microscope study. *Anal. Rec.* 252, 176–184.
- Rostrup, E., Law, I., Blinkenberg, M., Larsson, H.B., Born, A.P., Holm, S., Paulson, O.B., 2000. Regional differences in the CBF and BOLD responses to hypercapnia: a combined PET and fMRI study. *Neuroimage* 11, 87–97.
- Schreiner, W., Karch, R., Neumann, M., Neumann, F., Szawlowski, P., Roedler, S., 2005. Optimized arterial trees supplying hollow organs. *Med. Eng. Phys.* 28, 416–429.
- Schridde, U., Khubchandani, M., Joshua, E., Motelow, J., Sanganahalli, B.G., Hyder, F., Blumenfeld, H., 2008. Negative BOLD with large increases in neuronal activity. *Cereb. Cortex* 18, 1814–1827.
- Secomb, T.W., Hsu, R., Park, E.Y., Dewhurst, M.W., 2004. Green's function methods for analysis of oxygen delivery to tissue by microvascular networks. *Ann. Biomed. Eng.* 32, 1519–1529.
- Segal, S.S., Damon, D.N., Duling, B.R., 1989. Propagation of vasomotor responses coordinates arteriolar resistances. *Am. J. Physiol. Heart Circ. Physiol.* 256, H832–H837.
- Sheth, S.A., Nemoto, M., Guiou, M., Walker, M., Pouratian, N., Toga, A.W., 2004. Linear and nonlinear relationships between neuronal activity, oxygen metabolism, and hemodynamic response. *Neuron* 42, 347–355.
- Sheth, S.A., Nemoto, M., Guiou, M., Walker, M., Pouratian, N., Hageman, N., Toga, A.W., 2004b. Columnar specificity of microvascular oxygenation and volume responses: implications for functional brain mapping. *J. Neurosci.* 24, 634–641.
- Shmuel, A., Yacoub, E., Pfeuffer, J., Van de Moortele, P.F., Adriany, G., Hu, X., Ugurbil, K., 2002. Sustained negative BOLD, blood flow and oxygen consumption response and its coupling to the positive response in the human brain. *Neuron* 36, 1195–1210.
- Shmuel, A., Yacoub, E., Chaimow, D., Logothetis, N.K., Ugurbil, K., 2007. Spatio-temporal point-spread function of fMRI signal in human gray matter at 7 Tesla. *Neuroimage* 35, 539–552.
- Stefanovic, B., Hutchinson, E., Yakovleva, V., Schram, V., Russel, J.T., Belluscio, L., Koretsky, A.P., Silva, A.C., 2008. Functional reactivity of cerebral capillaries. *J. Cereb. Blood Flow Metab.* 28, 961–972.
- Thomason, M.E., Burrows, B.E., Gabrieli, J.D.E., Glover, G.H., 2005. Breath holding reveals differences in fMRI BOLD signal in children and adults. *Neuroimage* 25, 824–837.
- Turner, R., Thomas, D., 2006. Cerebral blood volume: measurement and change. *Proceedings of the 14th Scientific Meeting of the International Society for Magnetic Resonance in Medicine*, p. 2771 (A).
- Tuunanen, P.I., Kauppinen, R.A., 2006. Effects of oxygen saturation on BOLD and arterial spin labeling perfusion fMRI signals studied in a motor activation task. *Neuroimage* 30, 102–109.
- Tuunanen, P.I., Murray, I.J., Parry, N.R., Kauppinen, R.A., 2006. Heterogeneous oxygen extraction in the visual cortex during activation in mild hypoxic hypoxia revealed by quantitative functional magnetic resonance imaging. *J. Cereb. Blood Flow Metab.* 26, 263–273.
- Uludağ, K., Müller-Bierl, B., Ugurbil, K., 2009. An integrative model for neuronal activity-induced signal changes for gradient and spin echo functional imaging. *Neuroimage* 48, 150–165.
- Vafaee, M.S., Gjedde, A., 2004. Spatially dissociated flow-metabolism coupling in brain activation. *Neuroimage* 21, 507–515.
- Valabrégue, R., Aubert, A., Burger, J., Bittoun, J., Costalat, R., 2003. Relation between cerebral blood flow and metabolism explained by a model of oxygen exchange. *J. Cereb. Blood Flow Metab.* 23, 536–545.
- Vanzetta, I., Hildesheim, R., Grinvald, A., 2005. Compartment-resolved imaging of activity-dependent dynamics of cortical blood volume and oximetry. *J. Neurosci.* 25, 2233–2244.
- Villringer, A., Them, A., Lindauer, U., Einhäupl, K., Dirnagl, U., 1994. Capillary perfusion of the rat brain cortex: an in vivo confocal microscopy study. *Circ. Res.* 75, 55–62.
- Vogel, J., Kuschinsky, W., 1996. Decreased heterogeneity of capillary plasma flow in the rat whisker-barrel cortex during functional hyperemia. *J. Cereb. Blood Flow Metab.* 16, 1300–1306.
- Weber, B., Keller, A.L., Reichold, J., Logothetis, N.K., 2008. The microvascular system of the striate and extrastriate visual cortex of the macaque. *Cereb. Cortex* 18, 2318–2330.
- Woolsey, T.A., Rovainen, C.M., Cox, S.B., Henegar, M.H., Liang, G.E., Liu, D., Moskalenko, Y.E., Sui, J., Wei, L., 1996. Neuronal units linked to microvascular modules in cerebral cortex: response elements for imaging the brain. *Cereb. Cortex* 6, 647–660.
- Wu, G.H., Luo, F., Li, Z., Zhao, X.L., Li, S.J., 2002. Transient relationships among BOLD, CBV, and CBF changes in rat brain as detected by functional MRI. *Magn. Reson. Med.* 48, 987–993.
- Yablonsky, D.A., Haacke, M., 1994. Theory of MRI signal behavior in magnetically inhomogeneous tissues: the static dephasing regime. *Magn. Reson. Med.* 32, 749–763.
- Yacoub, E., Schmuel, A., Logothetis, N., Ugurbil, K., 2007. Robust detection of ocular dominance columns in humans using Hahn Spin Echo BOLD functional MRI at 7 Tesla. *Neuroimage* 37, 1161–1177.
- Yacoub, E., Harel, N., Ugurbil, K., 2008. High-field fMRI unveils orientation columns in humans. *Proc. Natl Acad. Sci. USA* 105, 10607–10612.
- Zheng, Y., Mayhew, J., 2009. A time-invariant visco-elastic windkessel model relating blood flow and blood volume. *Neuroimage* 47, 1371–1380.
- Zheng, Y., Martindale, J., Johnston, D., Jones, M., Berwick, J., Mayhew, J., 2002. A model of the hemodynamic response and oxygen delivery to brain. *Neuroimage* 16, 617–637.
- Zheng, Y., Pan, Y., Harris, S., Billings, S., Coca, D., Berwick, J., Jones, M., Kennerley, A., Johnston, D., Martin, C., Devonshire, I.M., Mayhew, J., 2010. A dynamic model of neurovascular coupling: implications for blood vessel dilation and constriction. *Neuroimage* 52, 1135–1147.

Lorthois, S., Cassot, F., Lauwers, F. Simulation study of brain blood flow regulation by intracortical arterioles in an anatomically accurate large human vascular network: Part II: Flow variations induced by global or localized modifications of arteriolar diameters., Neuroimage (2010), doi:10.1016/j.neuroimage.2010.10.040.

Supplementary figures

**Figure SM1: Global vasodilations: blood volume as a function of blood flow ( $d_{vaso}=9.9\mu\text{m}$  and  $H^{in}=0.4$ ).** All the data are normalized by their baseline value ( $f_{vaso}=0$ ). Circles: Case 1 without passive venous vasodilation; Squares: Case 2 without passive venous vasodilation. Plain lines: best adjustment of the data computed without passive venous vasodilation according to equations (5) and (6). Discontinuous lines: Grubb's law with  $\phi=0.30$  (fine line) and  $\phi=0.16$  (bold line). Upper panel: linear scale; lower panel: logarithmic scale.

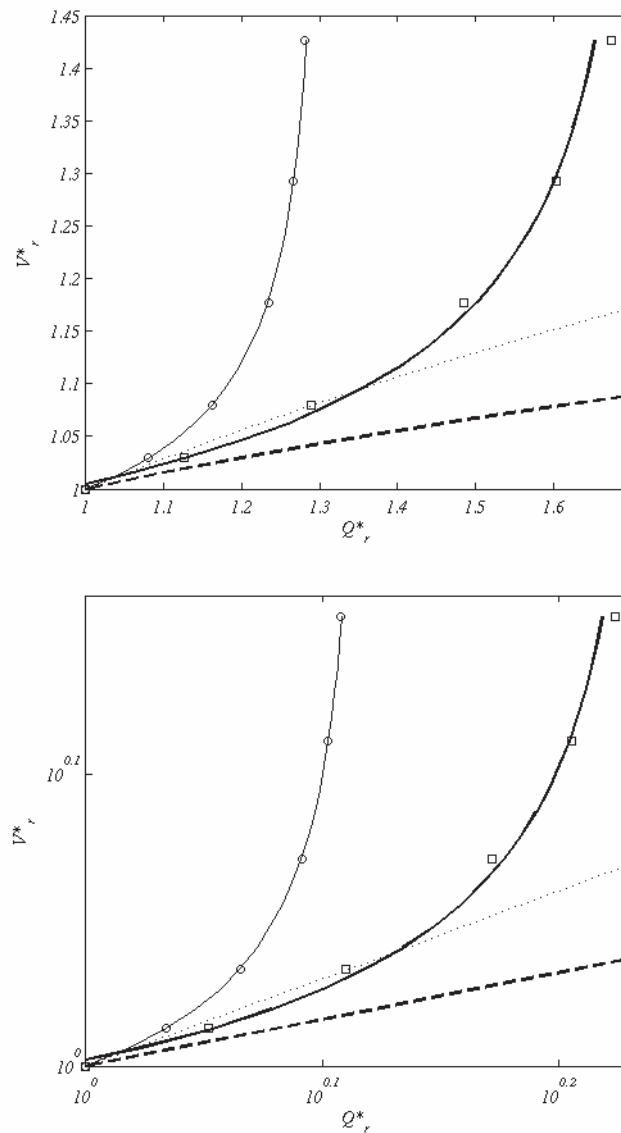




**Figure SM2: Maximal global vasodilation: Volume ( $V$ ) of arterial and venous territories as a function of blood flow in their vascular trunks to the power  $a$  ( $Q^a$ ).  $d_{vaso} = 9.9 \mu\text{m}$ .  $a$  was obtained by a linear fitting of  $V$  vs.  $Q$  in bi-logarithmic coordinates. Open symbols: veins; Filled symbols: arteries; Circles: Case 1; Squares: Case 2.**

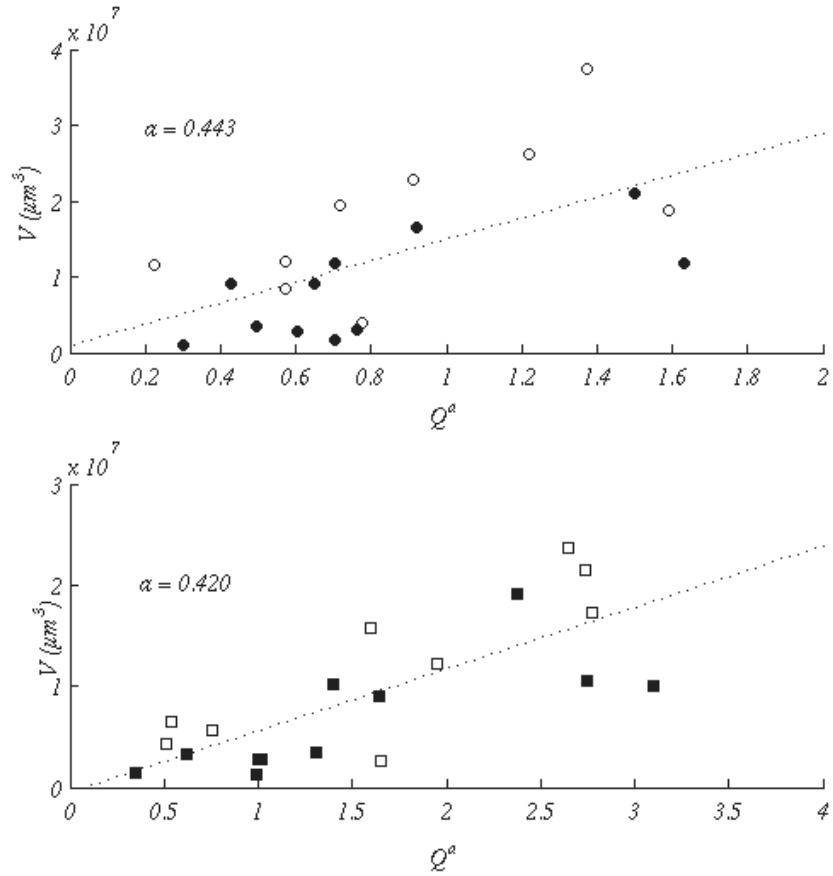


**Figure SM3: Maximal global vasodilation: Blood flow in parallelepiped ROIs following vasodilation plotted against the percentage of vascular volume occupied by arterioles or venules in the ROI.** Open symbols: 250  $\mu\text{m}$  ROIs; Filled symbols: 500  $\mu\text{m}$  ROIs; Circles: Case 1; Squares: Case 2. Note that, as the flow rate is a flux quantity, the flow rate in 500  $\mu\text{m}$  ROIs has been rescaled by a factor 6/16 to account for the difference in surface between a single 250  $\mu\text{m}$  ROI and a single 500  $\mu\text{m}$  ROI. The resulting points cloud (filled symbols) is reasonably included in the points cloud obtained for 250  $\mu\text{m}$  ROIs (open symbols) demonstrating the relevance of the observed correlation, which is indeed independent of the size of the ROI.  $H^{in}=0.4$ .

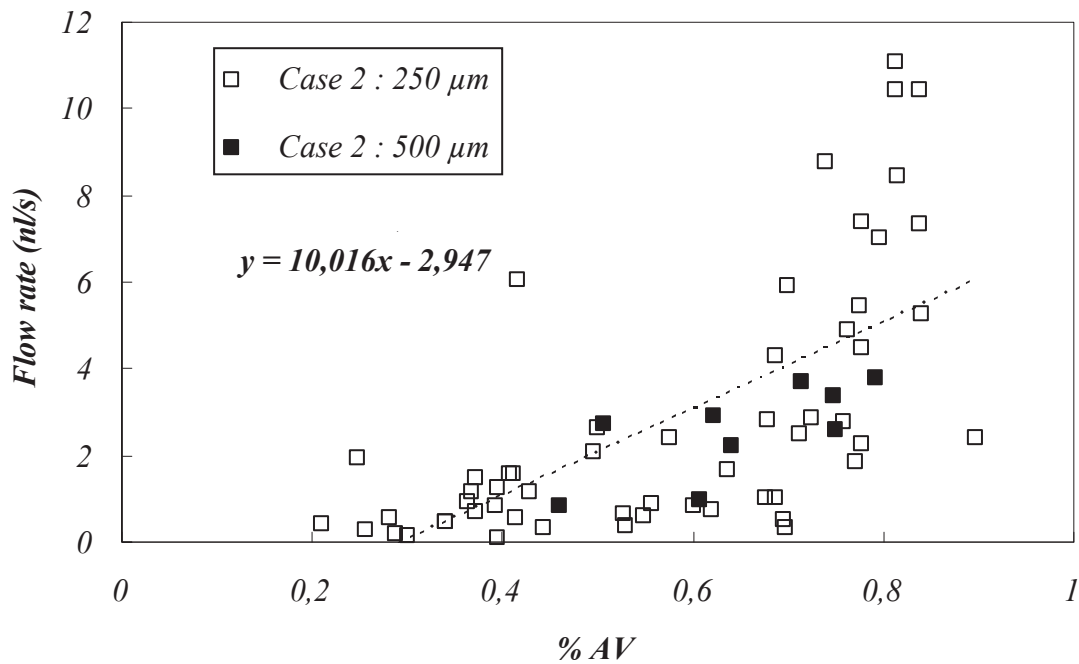
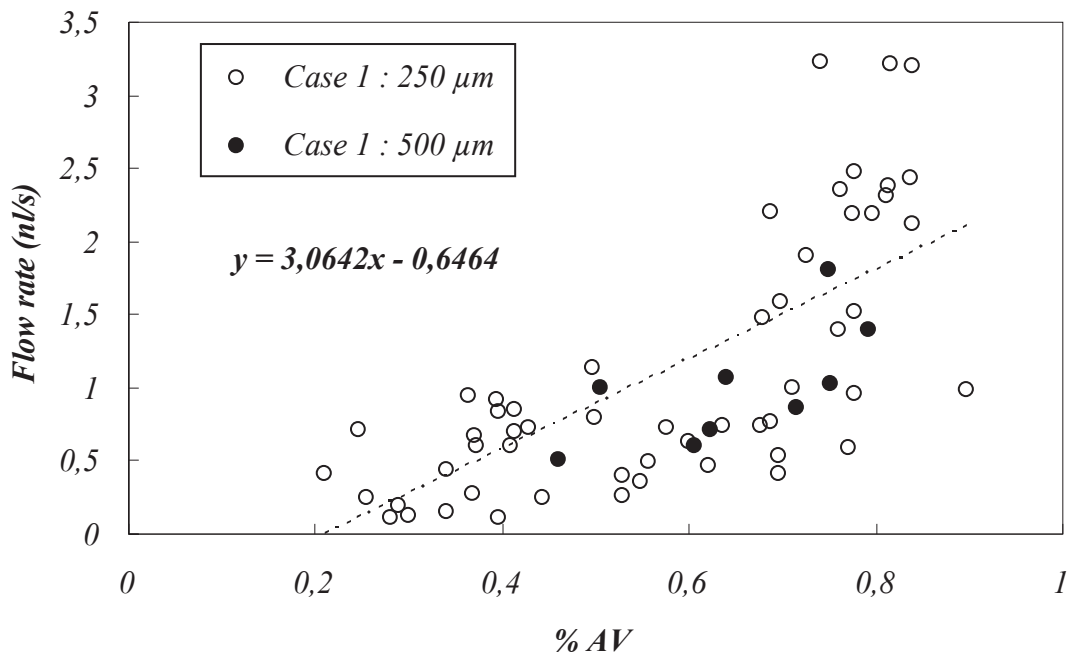


**Figure SM4 : Maximal global vasodilation: flow rate following vasodilation in each main arteriolar (open symbols) or venular trunk (closed symbols) as a function of baseline flow in the same trunks. Upper panel: Case1; Lower panel :Case 2. Plain (resp. dashed) lines are the best fits for the arterial (resp. venous) data. Dotted lines indicate the identity function.**

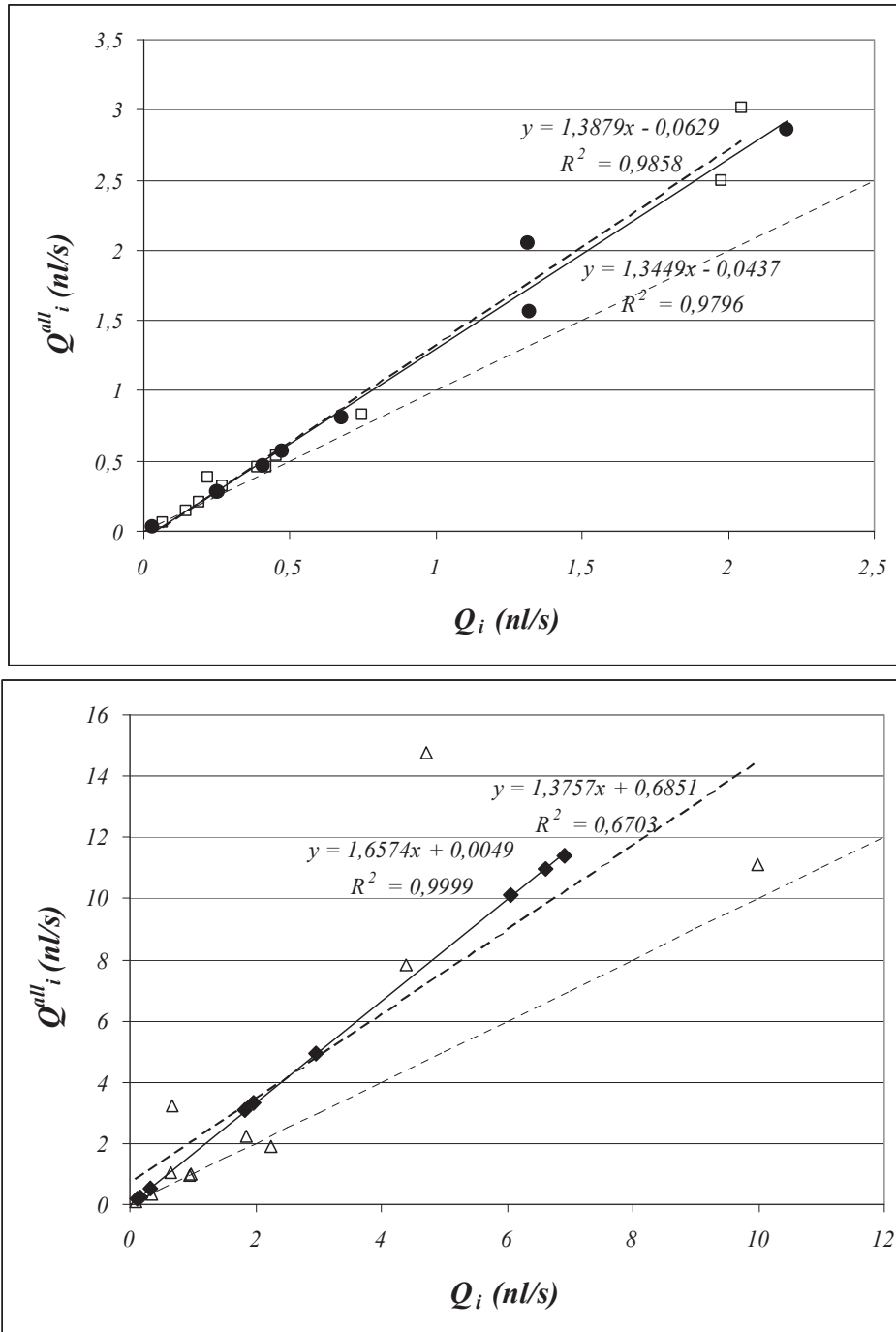


**Figure SM5: Maximal global vasodilation: volume of the territories of each main arteriolar (open symbols) or venular trunk (closed symbols) following vasodilation as a function of baseline volume of the same trunks. Same conventions as in Fig. SM4.**

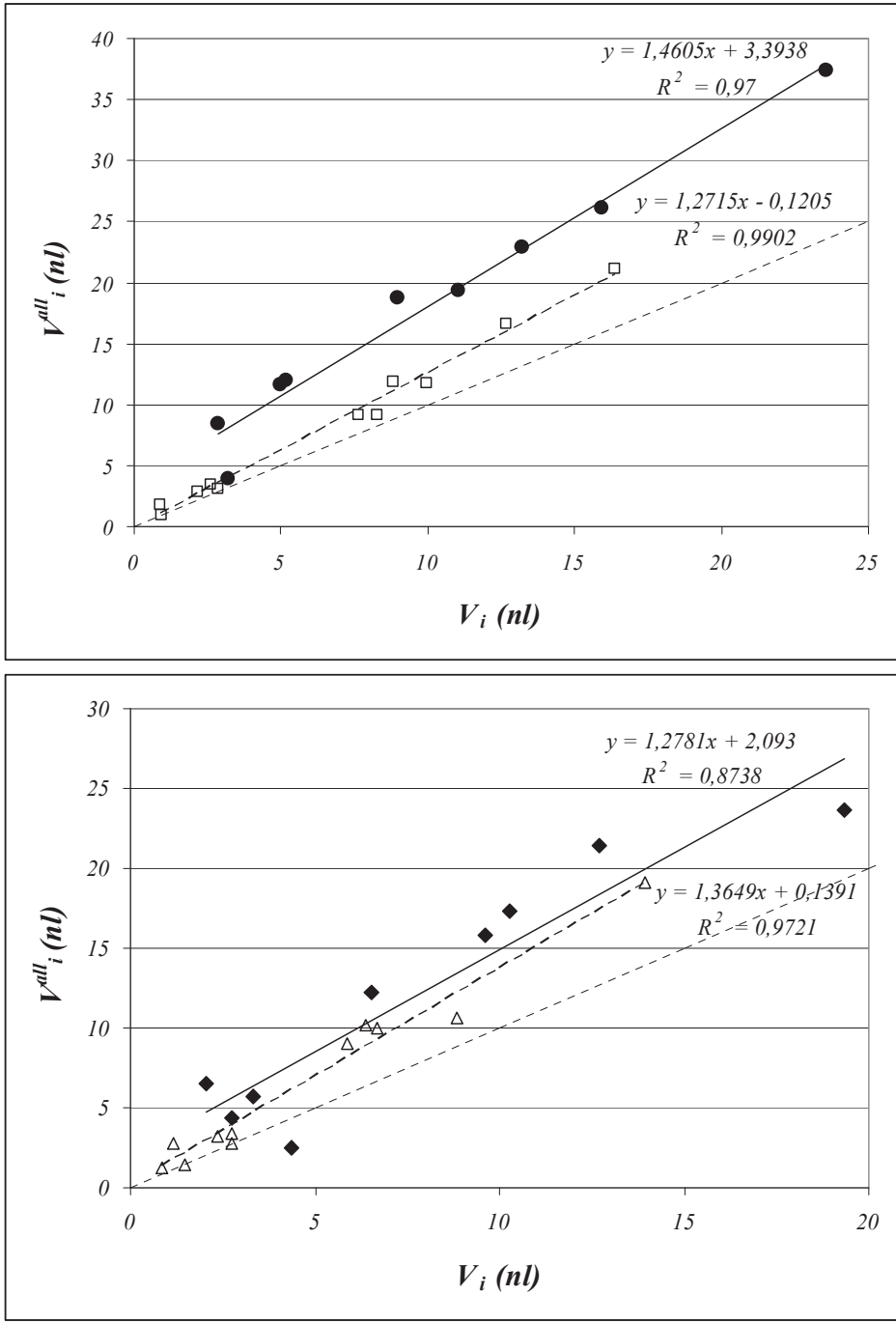


**Figure SM6: Maximal global vasodilation: relative variation of flow rate in each main arteriolar (open symbols) or venular trunk (closed symbols) compared to baseline as a function of baseline flow in the same trunks. Upper panel: Case1; Lower panel: Case 2.**

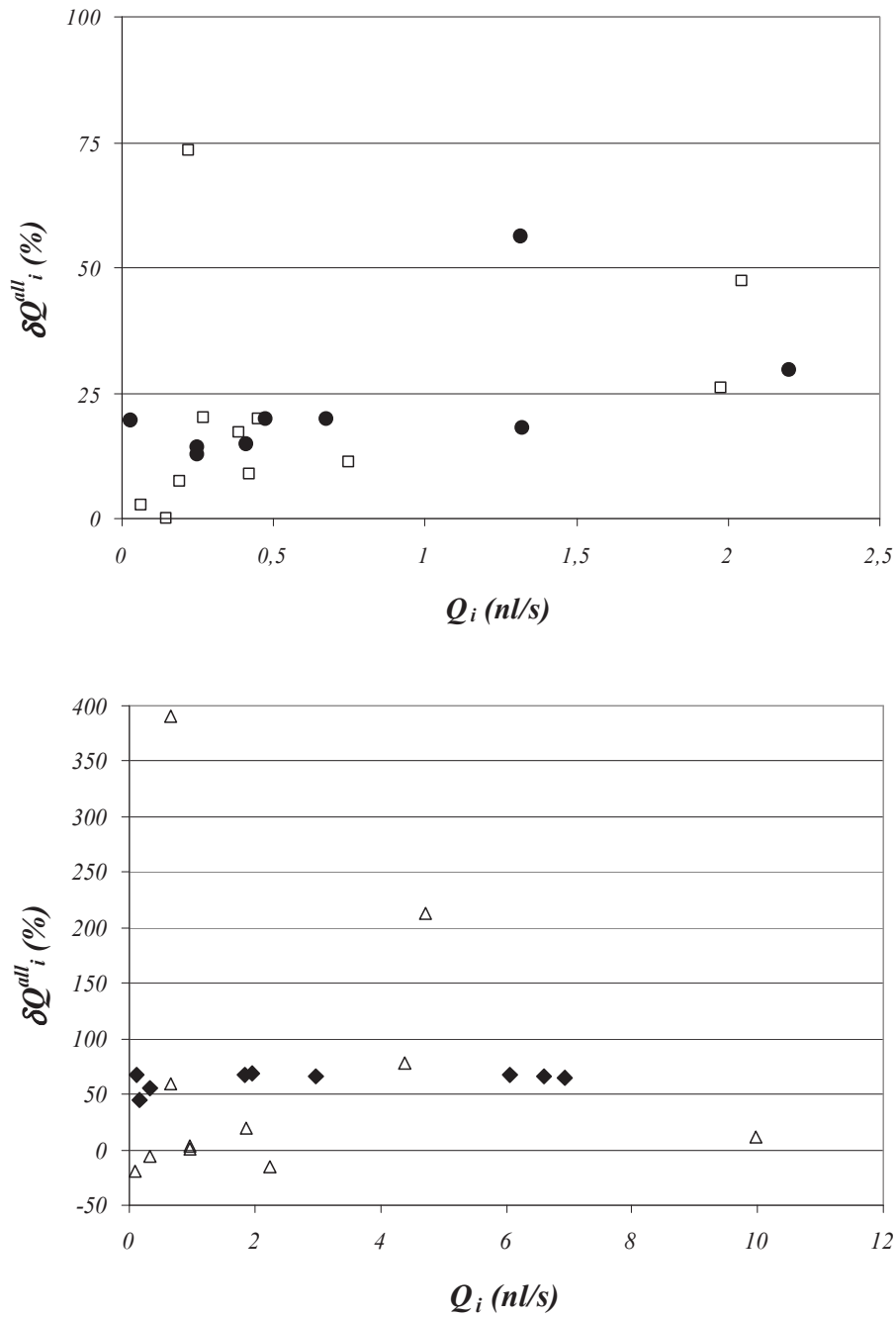


**Figure SM7: Maximal global vasodilation: relative variation of the volume of the territories of each main arteriolar (open symbols) or venular trunk (closed symbols) compared to baseline as a function of baseline volume of the same trunks. Same conventions as in Fig. SM6.**

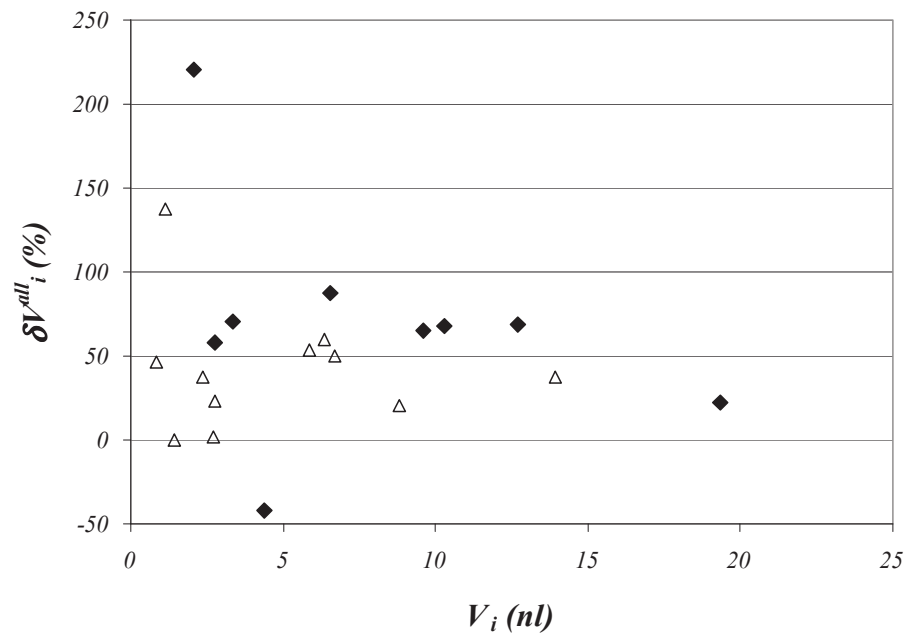
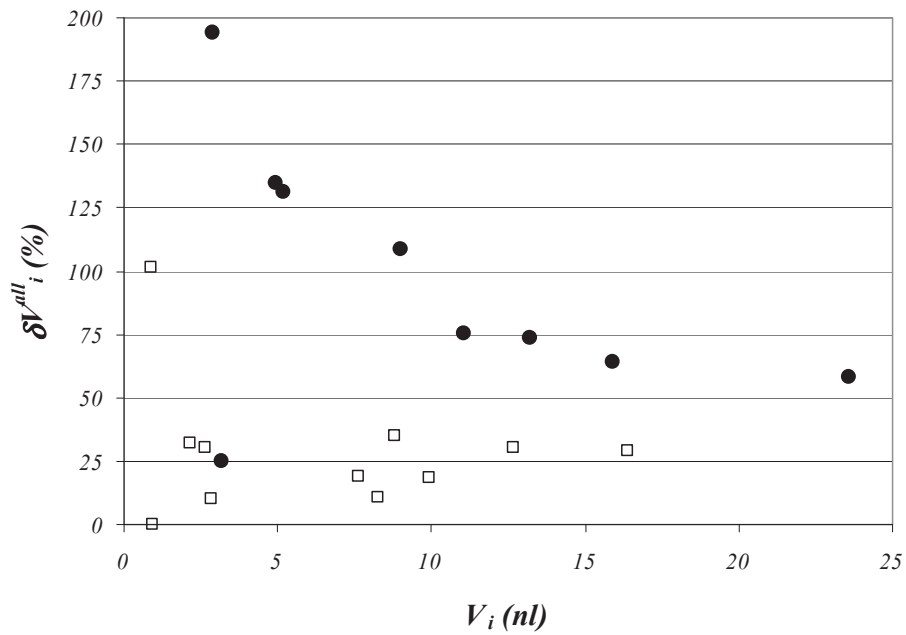


**Figure SM8: Maximal global vasodilation: flow rate following vasodilation in 250  $\mu\text{m}$  ROIs (open symbols) or 500  $\mu\text{m}$  ROIs (closed symbols) as a function of baseline flow in the same ROIs. Upper panel: Case1; Lower panel: Case 2. Dashed lines are the best fits for the 250  $\mu\text{m}$  data. Dotted lines indicate the identity function. Note that, as the flow rate is a flux quantity, the flow rate in 500  $\mu\text{m}$  ROIs has been rescaled by a factor 6/16 to account for the difference in surface between a single 250  $\mu\text{m}$  ROI and a single 500  $\mu\text{m}$  ROI.**

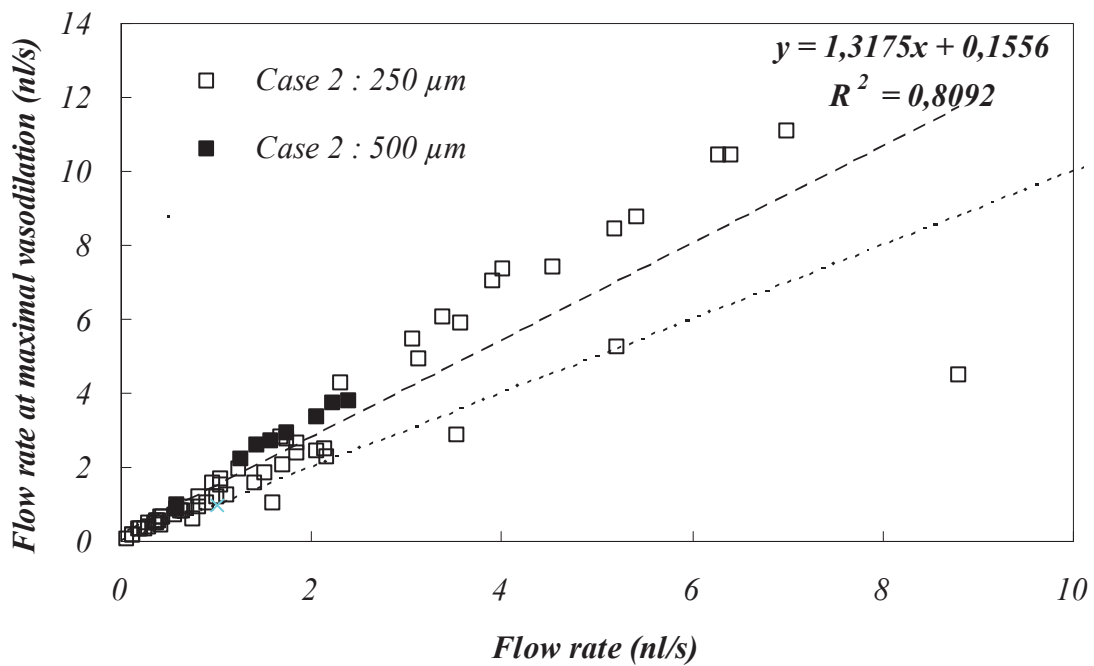
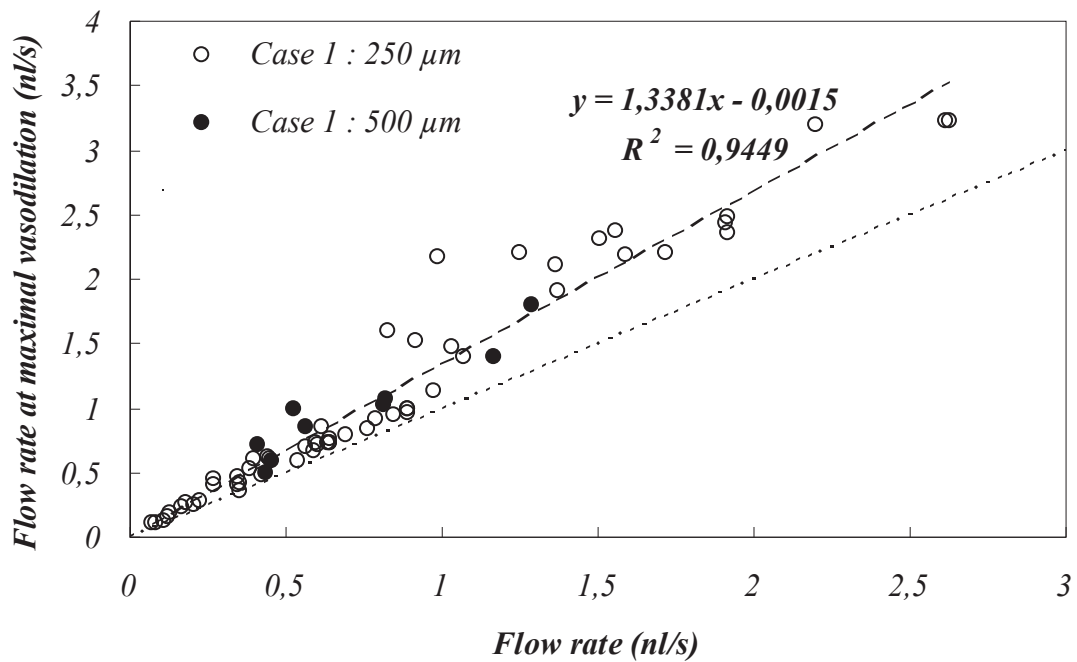


**Figure SM9: Maximal global vasodilation: relative variation of flow rate following vasodilation in 250  $\mu\text{m}$  ROIs compared to baseline as a function of baseline flow in the same ROIs. Upper panel: Case1; Lower panel: Case 2.**

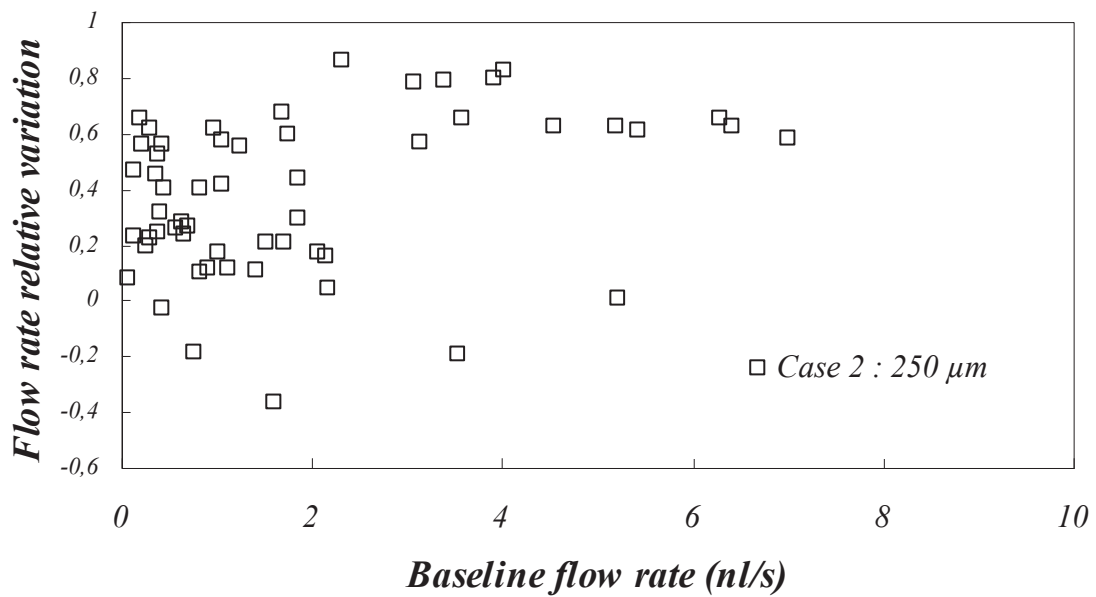
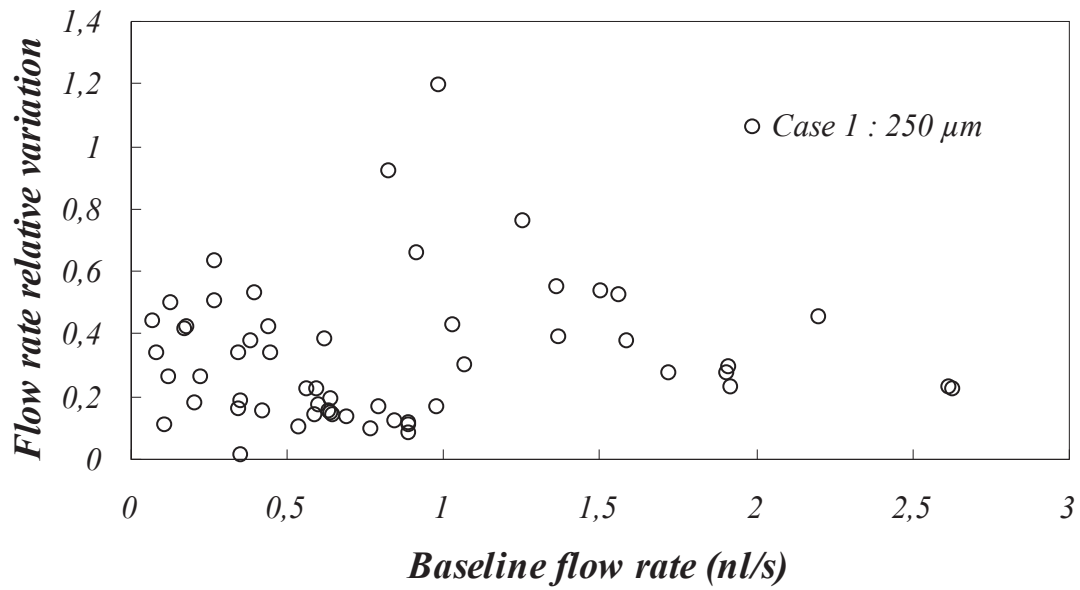




**Figure SM10: Maximal global vasodilation: relative variation of flow rate following vasodilation in 250  $\mu\text{m}$  ROIs compared to baseline as a function of relative variation of the proportion of vascular space occupied by non-capillary vessels in the same ROIs. Upper panel: Case1; Lower panel: Case 2.**

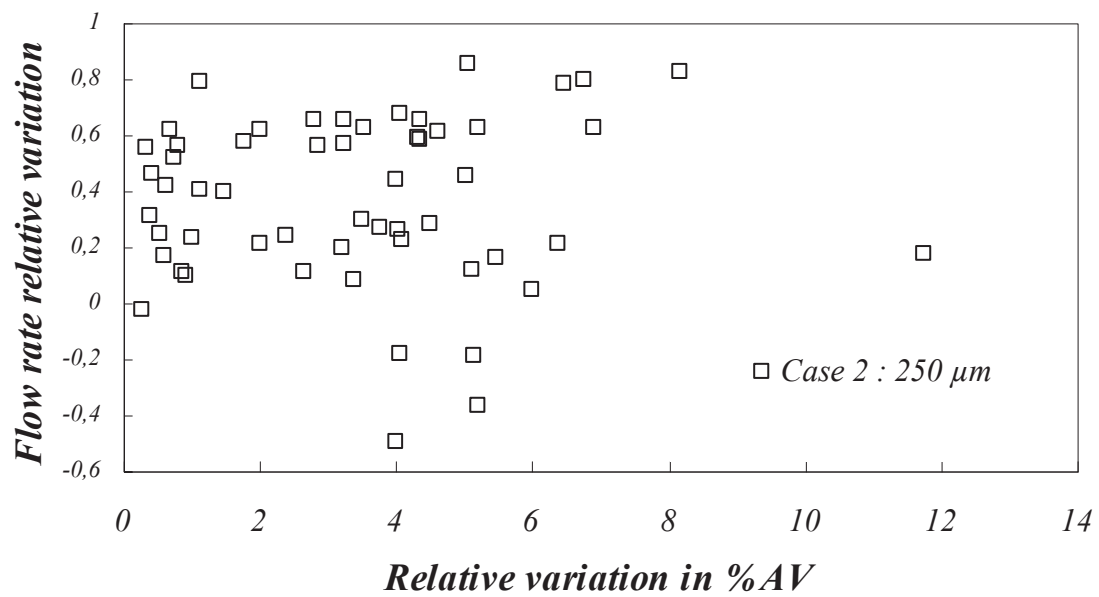
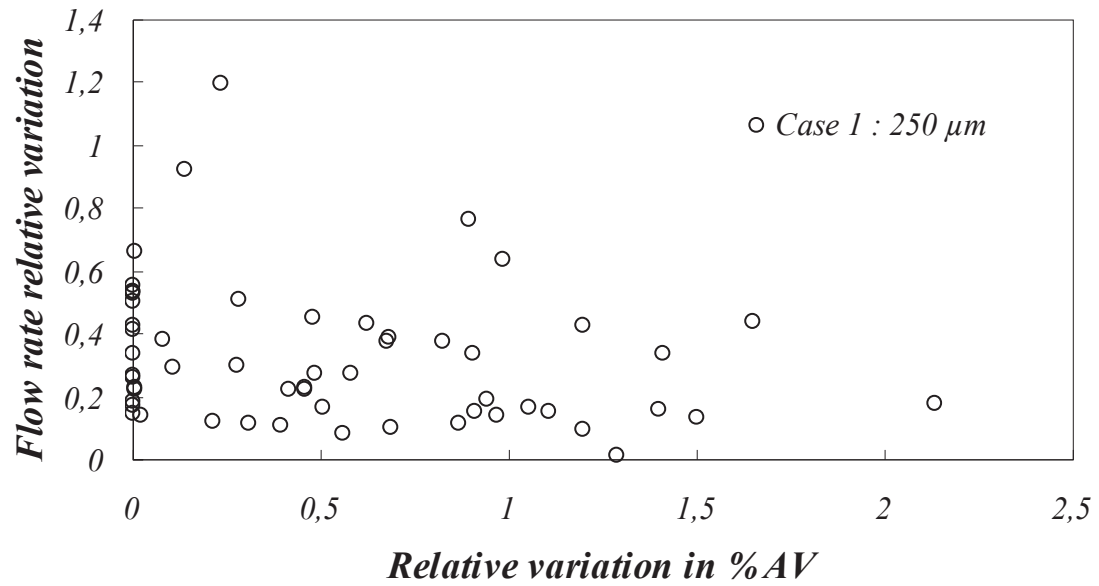


**Figure SM11: Flow rate (top) and volume of the arteriolar territory (bottom) of a given main arteriolar trunk (i) after localized vasodilation of this particular trunk (i) as a function of baseline values in the same trunk (i). The results obtained by “vasodilating” a different trunk each time are superimposed on the same graphs. Inserts display relative variations as a function of baseline value.**

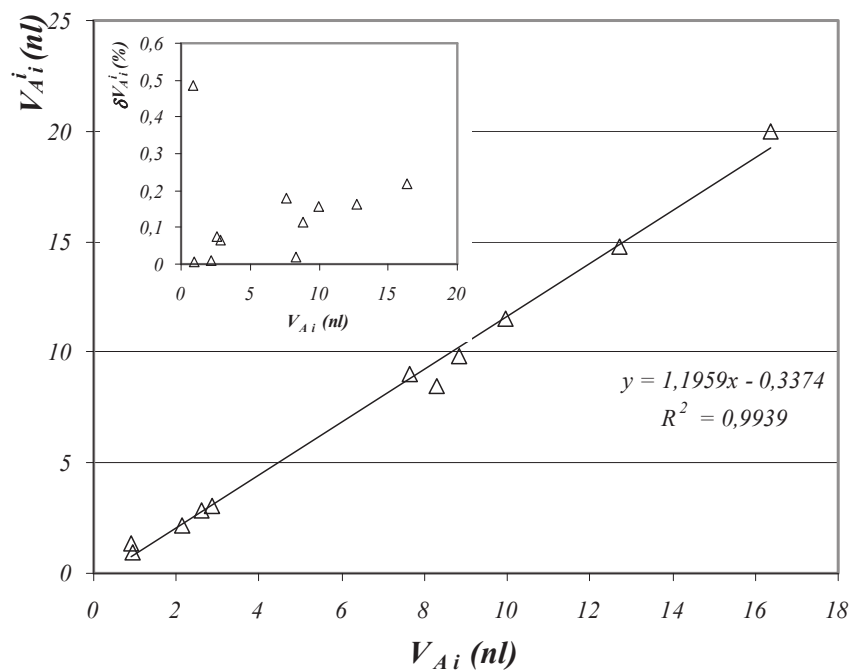
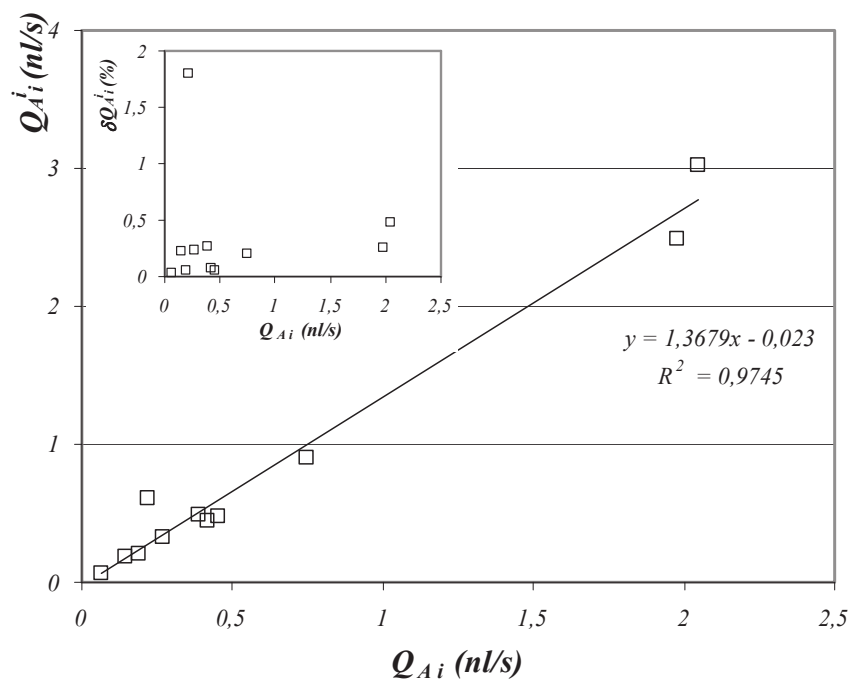


**Figure SM12: Global vasodilations: Normalized distributions of the relative pressure variations (left) and the relative flow rate variations (right) in the network between baseline ( $f_{vaso} = 1$ ) and maximal vasodilation ( $f_{vaso} = 2$ ). Case 1 : Continuous lines; Case 2 : dashed lines.**

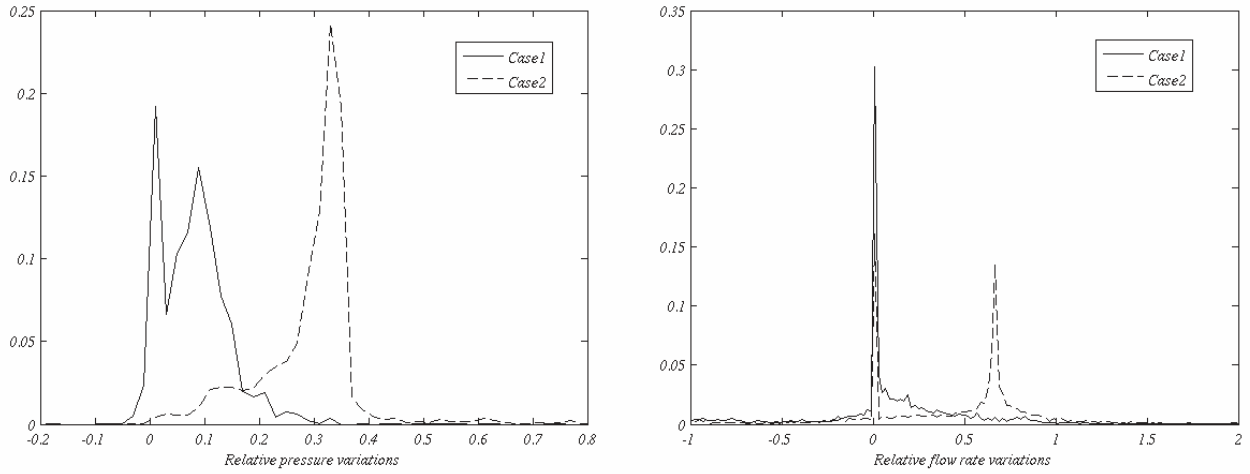


**Figure SM13: Local vasodilations: Normalized distributions of the relative pressure variations (left) and the relative flow rate variations (right) in the network between baseline ( $f_{vaso} = 1$ ) and maximal vasodilation ( $f_{vaso} = 2$ ). Vasodilation of arteriole *a*: dotted lines; Vasodilation of arteriole *b*: continuous lines; Vasodilation of arteriole *d*: dashed lines. NB: the frequency scale is in logarithmic coordinates.**

